# Cohesion and Initial Porosity of Granular Fault Gouges control the Breakdown Energy and the Friction Law at the Onset of Sliding

Nathalie Casas[1], Guilhem Mollon[1], and Ali DAOUADJI[2]

[1]INSA Lyon, LaMCoS
[2]INsa Lyon, GEOMAS

November 23, 2022

**Abstract**

Earthquakes happen with frictional sliding, by releasing excess stresses accumulated in the pre-stressed surrounding medium. The geological third body (i.e. fault gouge), originating from the wear of previous slips, contribute to friction stability and plays a key role in the energy released. An important part of slip mechanisms are influenced by gouge characteristics and environment. The study of several types of gouge, as mixtures of different initial porosity and cohesive contact law, allows to link fault gouge properties to its rheological behavior. In this paper, a cohesive fault gouge segment is modeled in 2D with DEM. The analyses of friction coefficient evolution, gouge kinematics and force chains within the gouge highlight the main mechanisms acting on fracture processes. A link is made between the initial state of the gouge and the ductile or brittle character of the whole granular flow. For the investigated data range, three regimes are highlighted: a mildly cohesive regime (ductile behavior), a cohesive regime with agglomerates formation and Riedel shear bands and an ultra-cohesive regime with several Riedel bands followed by ultra-localization (brittle behavior). As a result of this study, the total macroscopic friction generated during the shearing is proposed to be a combination of three contributions: Coulomb friction, dilation and decohesion process. A simplified model is built up to represent these contributions and to be implemented in dynamic rupture modelling at higher scale. The Breakdown energy appears to be controlled by the intensity of these three mechanisms and their associated slip distance.

# Cohesion and Initial Porosity of Granular Fault Gouges control the Breakdown Energy and the Friction Law at the Onset of Sliding

**N. Casas [1,2], G. Mollon[1], and A. Daouadji[2]**

[1] Univ. Lyon, INSA-Lyon, CNRS UMR5259, LaMCoS, F-69621, France.

[2] Univ. Lyon, INSA-Lyon, GEOMAS, F-69621, France.

Nathalie Casas (nathalie.casas@insa-lyon.fr)

**Key Points:**

- We simulate the onset of sliding of a granular fault gouge to link gouge properties to rheological behavior, using 2-D DEM
- A new partition of Friction and Breakdown energy is proposed as the sum of three contributions: Coulomb friction, Dilation and Decohesion.
- Three main granular regimes are observed with the increase of cohesion, showing an evolution from ductile to brittle behavior.

## Abstract

Earthquakes happen with frictional sliding, by releasing excess stresses accumulated in the pre-stressed surrounding medium. The geological third body (i.e. fault gouge), originating from the wear of previous slips, contribute to friction stability and plays a key role in the energy released. An important part of slip mechanisms are influenced by gouge characteristics and environment. The study of several types of gouge, as mixtures of different initial porosity and cohesive contact law, allows to link fault gouge properties to its rheological behavior. In this paper, a cohesive fault gouge segment is modeled in 2D with DEM. The analyses of friction coefficient evolution, gouge kinematics and force chains within the gouge highlight the main mechanisms acting on fracture processes. A link is made between the initial state of the gouge and the ductile or brittle character of the whole granular flow. For the investigated data range, three regimes are highlighted: a mildly cohesive regime (ductile behavior), a cohesive regime with agglomerates formation and Riedel shear bands and an ultra-cohesive regime with several Riedel bands followed by ultra-localization

(brittle behavior). As a result of this study, the total macroscopic friction generated during the shearing is proposed to be a combination of three contributions: Coulomb friction, dilation and decohesion process. A simplified model is built up to represent these contributions and to be implemented in dynamic rupture modelling at higher scale. The Breakdown energy appears to be controlled by the intensity of these three mechanisms and their associated slip distance.

## 1. Introduction

During an earthquake, frictional sliding releases the stresses accumulated in the pre-stressed surrounding medium. The fault gouge identified as the wear material of previous slips, contribute to friction stability and plays an important role in the sudden energy release at the onset of seismic sliding. Gouge characteristics (rock, particle size, friction…) and constrained environment (pressure, slip velocity…), are believed to influence, if not control, a large part of slip mechanisms. Such gouge parameters have been studied in the literature from Lab or in-situ point of view [(Byerlee & Brace, 1968), (C. Sammis et al., 1987), (Biegel et al., 1989), (Marone & Scholz, 1989), (Mair & Marone, 1999), (Anthony & Marone, 2005)] and also numerically by the mean of Discrete Element Modelling (DEM). This technique, prominent in granular mechanics and physics, has shown its ability to represent granular gouges in several studies [(Morgan & Boettcher, 1999), (Morgan, 1999), (Guo & Morgan, 2004), (Da Cruz et al., 2005), (Cho et al., 2008), (Zhao et al., 2012), (Gao et al., 2018)], but remains underutilized in the field of fault mechanics despite its large potential.

However, gouge material properties also depend on the maturity of the fault and thus on its cohesion and porosity state. The number of slips occurring within the gouge reduces the size of particles towards a fractal distribution, which also reduces pore spaces [(C. G. Sammis & Biegel, 1989), (Blenkinsop, 1991), (Muto et al., 2015)]. This particle size distribution can be explained by grain breakage [(Daouadji et al., 2001), (Daouadji & Hicher, 2010)]. Within a mature fault gouge, mineral cementation coming from rock dissolution, melting or other processes derived from previous slips, can fill remaining pore spaces between particles and change the global state of cohesion (Philit et al., 2018). (Lade & Overton, 1989) showed that, for low confining pressures, the increase of cementation and the associated tensile strength lead to an enhancement of friction coefficient. This phenomenon gives birth to a new stronger granular material combining its history, the state of initial density (i.e. porosity within the sample) and the cementation (Schellart, 2000).

In DEM, where such a deformable matrix can hardly be implicitly represented, this cementation can be schematized by cohesive and breakable links between particles. Bonded Particle Models are often used to represent cohesive laws within granular rocks [(Potyondy & Cundall, 2004), (Cho et al., 2007)].

Cohesion is a difficult parameter to observe and to quantify and even more to follow during experiments, but some papers have already tried to describe it with granular and rheology studies, especially in the fields of soil mechanics and tribology. (Rognon et al., 2008) studied the influence of cohesion on dense granular material and explained that the increase of cohesion enhances the agglomeration of particles, changing the total shear resistance. Similar results have been found by (Mollon, 2019) with deformable material. (Iordanoff et al., 2005) demonstrate that the loss in homogeneity created by agglomerates also makes the material more brittle.

Energy budget of earthquakes (based on slip weakening theory) is composed of a frictional energy dissipated within the slip zone $E_H$, a radiated energy $E_r$ propagating with elastic waves and an energy $E_G$ coming from fracturing process [(Kanamori & Heaton, 2000), (Abercrombie & Rice, 2005)]. $\Delta W$ is the total deformation energy dissipated in the process, and is the sum of the three previous terms. (Chester et al., 2005) found that fracture energy $E_G$ is small compared to the other energies. However small, this energy is needed to weaken a fault during an earthquake and to allow fracture propagation, and local mechanisms contributing to $E_G$ are not well defined in literature.

Slip weakening literature reports a large range of phenomena. The first type of weakening is linked to heating phenomena. They mainly occur under high pressure and velocity, within a very thin slipping zone, and need a certain amount of sliding before occurring. The temperature rise can lead to melting [(Giulio Di Toro et al., 2006) & (Niemeijer et al., 2011)] or fluid pressurization (J. R. Rice, 2006). These heating processes are related to a large mechanical work rate within the slip zone (G Di Toro et al., 2011). The well known critical slip distance $D_c$ becomes negligible before the thermal slip distance $D_{th}$ obtained (in the order of the meter for lab experiment and extrapolated to the order of centimeter for real faults). Another contribution to weakening is related to fracture mechanics and slipping zone. A slip weakening is observed from static to dynamic friction state, and mainly based on surface geometry, particles topography and contact properties. The main slipping zone can contain cohesive or non-cohesive wear material (J. Rice & Cocco, 2005), and a millimetre scale slip distance is observed.

The main objective of this paper is to establish a link between properties of the gouge layer (geological, mechanical, physical…) and its rheological behaviour. Varying the percentage of cohesion within the gouge, for different initial porosities, leads to a wide range of mechanical behaviours that we can compare to fault rupture theory. In order to isolate the main mechanisms acting on fracture processes, we propose a new partition of the total macroscopic friction generated during the shearing of a granular gouge. The first section introduces a dry cohesive fault segment model in 2D (2x20mm²) involving two rough surfaces representing the rock walls separated by the granular gouge. This paper proposes to use DEM on angular and faceted grains as we can find in real granular fault gouge (Olgaard & Brace, 1983). Focusing on physics of contacts inside the granular medium, we explore friction coefficient evolution, gouge kinematics and force chains within the gouge in a second section. We aim in this section to study the effect of cohesion and porosity on mechanical behaviours and slip triggering. This second section also presents a new decomposition of sliding friction into three main contributions: the rupture of cohesive bonds, the dilatancy of the gouge and Coulomb dissipations due to friction. The last section describes new insights and relation between cohesion within the gouge, shear localisations and fracture energy evolution.

## 2. Numerical modelling and sample generation

A 2D granular fault gouge model is implemented in the framework of Discrete Element Modelling (DEM) in the software MELODY (Mollon, 2016). Since DEM was first proposed by (Cundall & Strack, 1979), it has been applied several times [(Morgan & Boettcher, 1999), (Guo & Morgan, 2004), (Da Cruz et al., 2005), (Ferdowsi et al., 2014), (Dorostkar et al., 2017a), (Gao et al., 2018)] to the simulation of micro-scale behaviours inside the fault gouge. It is indeed commonly accepted that granular phenomena within the gouge drive a large part of physics of slip triggering.

MELODY 2D (Multibody ELement-free Open code for DYnamic simulation) is a C++ code allowing to simulate any kind of granular media. In contrast with conventional codes, it is able to deal with any 2D shape and behaviour of particles, from rigid circular to highly compliant angular grains (this latter case is outside of the strict DEM framework, and uses a Multibody Meshfree Approach). As in classical DEM codes, each particle has its own movement and trajectory, driven by Newton's laws of motion and controlled by user-defined and physics-based contact interactions and constitutive laws inside the sample [(Mollon, 2018a) & (Mollon, 2018b)].

### 2.1. Generation of granular gouge sample

Mineral grains morphologies can be very diverse, but granular gouges generated by comminution are expected to exhibit rather rough and angular shapes [(Olgaard & Brace, 1983), (An & Sammis, 1994), (Lin, 1999)]. Many studies [(Mair et al., 2002), (Nouguier-lehon et al., 2003), (Guo & Morgan, 2004), (Anthony & Marone, 2005)] have shown that using angular and faceted shapes instead of circular grains led to higher friction coefficients and different global behaviours. For 3D laboratory experiments with real grains, steady-state macroscopic friction is usually around 0.6 (Mair et al., 2002), in opposition to spherical particles with a macroscopic friction that rarely exceeds 0.45. Because of their invariance by rotation, smooth spherical shapes tend to roll to accommodate deformation of the grain assembly whereas interlocking between angular grains tends to promote dilation. It was also shown recently that mechanical effects of grains surface roughness can only be mimicked by intergranular friction to a certain extent, and that a proper modelling of the shear behaviour of granular samples requires realistic shapes (Mollon et al., 2020).

The Matlab package Packing2D (Mollon & Zhao, 2012) is employed to create a realistic granular sample. It is based on a Fourier-Voronoï method and generates a set of angular and faceted grains with a user-defined size distribution and a control on key morphological descriptors (such as elongation, circularity, and roundness). This control is performed by choosing a Fourier spectrum that quantifies the frequencies and amplitudes of the grain surface asperities. Since the morphological descriptors of the grains of granular gouges may vary significantly between faults, we calibrate our spectrum by visual comparison with published pictures of real gouges (Figure 1. (a) – (b)).

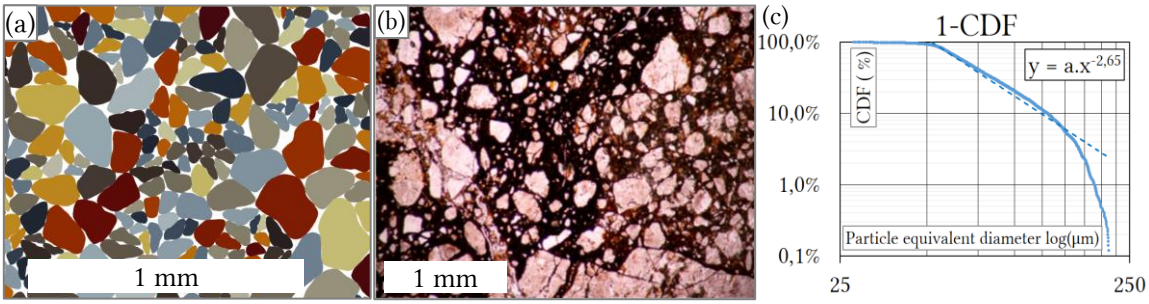


**Figure 1**. (a) Granular sample generated with packing2D, with angular and faceted shapes, and compacted in MELODY2D (b) Quartz, photomicrograph (crossed polars) of ATTL fault gouge from (Muto et al., 2015) (c) Log–

log graphs showing the cumulated number of particles (Y-axis) plotted against particle equivalent diameters (X-axis) from the numerical gouge sample with CDF (Cumulative Distribution Function). The fractal dimension D equals 2.65.

The thickness of the shearing zone should be between 1 and 5 mm (J. Rice & Cocco, 2005). Regarding the literature, we create a 2mm-thick granular fault gouge and determine what length is needed to obtain a Representative Surface Element (RSE), (supporting information S2). A gouge of 2 x 20 $mm^2$ is found to be satisfactory and falls within the same order of magnitude as previous studies [(Ferdowsi, 2014) & (Dorostkar et al., 2017b)]. The fractal size distribution is chosen to fit with literature on granular gouge composition, [(Olgaard & Brace, 1983), (Blenkinsop, 1991), (Billi & Storti, 2004), (Billi, 2005), (Muto et al., 2015)], with a fractal dimension factor D close to 2.6. The gouge is composed by 4960 particles with a corresponding equivalent diameter in the range 28 – 260 μm (average value of 81 μm) and a (D50) equal to 70 μm (Figure 1– c).

### 2.2. Direct shear modelling

In addition to the granular gouge, the model is completed by adding rock walls at the top and bottom sides of the granular sample (Figure 2). Contact surfaces of rock walls are sinusoidal in order to introduce a certain roughness and avoid wall-slip effects, since we want to ensure that slip accommodation takes place within the gouge. The lower wall is fixed, while a normal stress of 40 MPa is applied on the upper rock wall. Gravity is ignored in the model, assuming that the fault can be oriented in a wide range of directions, and that gravity forces are negligible compared to those related to normal and deviatoric stresses applied on the gouge.

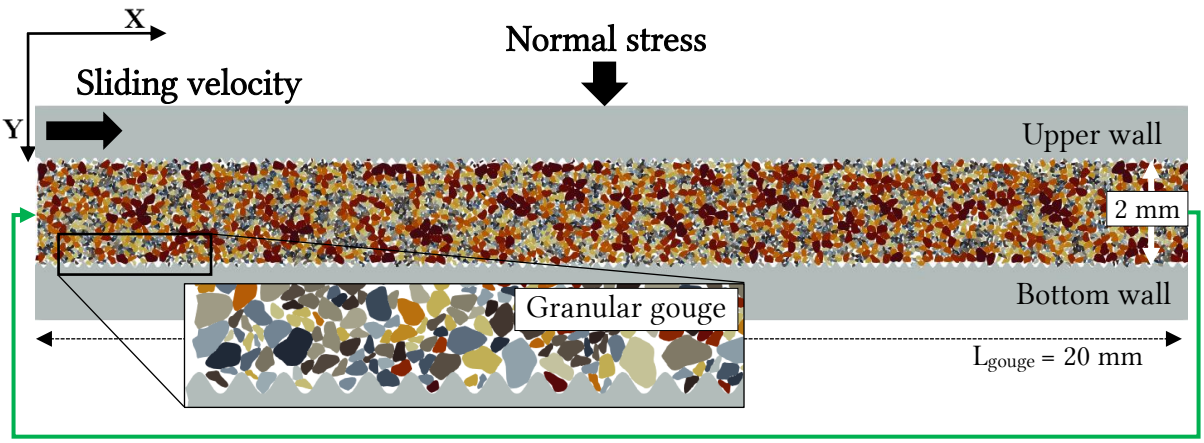


**Figure 2**. DEM model of a granular fault gouge, 4960 angular particles in a 2x20mm domain.

The first simulation stage consists in compacting the gouge with a temporary intergranular friction coefficient that is chosen in order to control the initial porosity of the sample (noted $P_s$ and defined as the ratio of the surface occupied by voids to the apparent surface of the sample). We keep two different initial porosities for this study, ($P_s$=16%) for mid-dense sample and ($P_s$=11%) for dense samples (Supporting information S3 for more explanations). After compaction and stabilization, the contact law between grains is modified by the introduction of cohesion between particles (see next subsection) and a 1m/s slipping rate is applied on the upper rock wall. This high velocity allows the simulations to run in a reasonable amount of time while avoiding disturbing inertial effects, since the inertial number in that case is close to 1e-3 (i.e. quasi-static dense granular flow according to (Da Cruz et al., 2005)). The movement of the upper rock wall in the y-direction is free in order to allow gouge dilatancy. Periodic boundary conditions are present on both right- and left-hand sides of the sample to maintain the continuity of the movement at large slips. In this study, we choose to simulate a granitic rock with a volumetric mass of 2600 kg/m$^3$ for particles. An explicit solver is used (Symplectic Euler scheme), to integrate in time the motion of each body. (Numerical setup and parameters are summuerized in supporting information S1.)

### 2.3. Contact laws

We consider a dry cohesive contact model to investigate cohesion mechanism of dry gouges. Cohesion is used here to simulate a mature fault gouge with mineral cementation between particles. Fault gouge and rock walls are considered as rigid with no body deformation allowed, but a numerical stiffness is used to limit interpenetration between grains while mimicking the local

deformation of the grains in the contact vicinity. Hertz contact law prescribes a non-linear contact stiffness, but for the sake of simplicity, we adopt a constant value of 1e15 N/m$^3$ in order to obtain an overall deformability of the sample of the same order of magnitude as the one for bulk granite. Inter-particle friction is equal to 1 at the contact interface between walls and particles to make sure that the motion is fully-coupled at the wall-grains transition. For inter-particle contacts, friction equals 0.5, a value close to the ones observed in literature for steady-state behaviour (Mair et al., 2002).

To represent grain cementation, a Bonded Mohr-Coulomb law is applied, considering for the sake of simplicity that inter-particle bridges and particles are made with the same material. This contact law is close to the Bonded-Particle-Model (BPM) from (Potyondy & Cundall, 2004) and presents two main status (intact or broken) described below.

Since the contour of each grain is discretized by a piecewise linear frontier with nodes and segments, each contact considered in the code concerns a given node from a grain A and a given segment from a grain B. From this node and this segment, we can at any moment compute a normal gap $\delta_n$ (obtained by projecting the node on the segment) and a tangential gap $\delta_t$ (integrated in time based on the history of the relative motions of the node and the segment in the tangential direction). $\delta_n$ can be either negative (i.e. there is a small interpenetration between the grains) or positive (i.e. there is a separation distance between the grains). This contact algorithm is described in more details in (Mollon, 2018a). These two gaps are used to compute the contact forces, based on the following rules:

(a) After compaction and before shearing, all contacts for which $\delta_n < (\delta_{detection} = C_{num}/k)$ (where $k$ is the contact stiffness and $C_{num}$ is the numerical cohesion) are attributed the status "intact" (Figure 3 – a).

↳ If a contact is "intact", the following contact stresses are computed based on a purely cohesive contact law:

$$\sigma_n = k\delta_n \quad (2.3.1)$$

$$\sigma_t = k\delta_t \quad (2.3.2)$$

↳ If [$\sigma_n$ or $abs(\sigma_t)$] exceeds the prescribed value of cohesion $C_{num}$, the status of the contact is updated to "broken" (Figure 3 – b).

(b) If a contact is "broken", (Figure 3 – b), either because it is a former intact bond or because it is newly created by grains motions at any time in the simulation, the following contact stresses are computed based on a purely frictional contact law:

$$if\ (\delta_n > 0)\ \rightarrow \qquad \sigma_n = \sigma_t = 0 \tag{2.3.3}$$

$$if\ (\delta_n < 0)\ \rightarrow \quad \begin{cases} \sigma_n = k\delta_n & (2.3.4) \\ \sigma_t = min(k\delta_t, \mu\delta_n) & (2.3.5) \end{cases}$$

Where $\mu$ is a contact friction coefficient.

From these stresses, the associated contact forces (in the normal and tangential direction, as well as the associated torque) are computed on each grain, by considering that contact stresses act on a contact length $L_c$ (equal to the sum of half-lengths of the segments around contact nodes in grain A):

$$F_n = L_c\ \delta_n \tag{2.3.6}$$

$$F_t = L_c\ \delta_t \tag{2.3.7}$$

These laws are completed by a classical viscous dashpot in order to dissipate kinetic energy by contact damping and to stabilize the simulation.

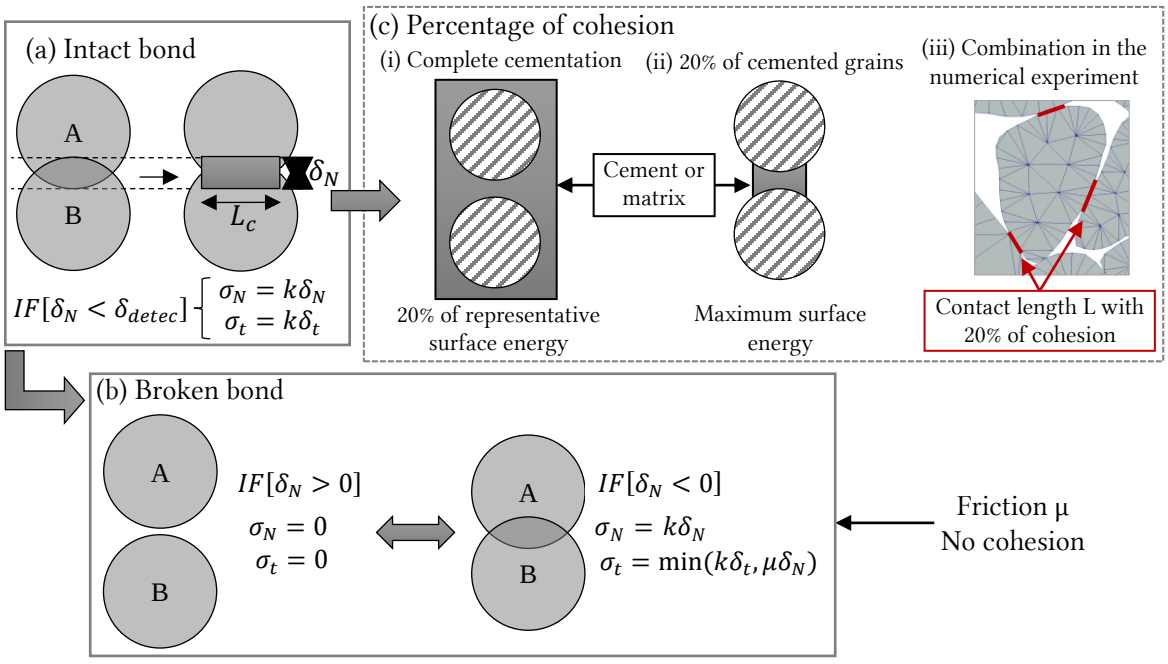


**Figure 3**. (a) Initialisation of the contact law. A cohesive law links all grains in contact. The bond corresponds to a constant pressure to maintain particles in contact (Pa). (b) When the force applied on the particles becomes higher than the cohesive link, the bond is broken. The contact becomes cohesionless and follows a classical Mohr-Coulomb law

with inter-particle friction only. Broken contacts cannot be cohesive again and this induces an augmentation of broken bonds during the shearing. (c) Sketch of the percentage of cohesion in the sample for intact bond and an illustrative cohesion of 20%: (i) complete cementation but with 20% of the reference surface energy, (ii) reference surface energy but cemented bonds on only 20% of grains contours in average, (iii) Combination of the two previous cases in numerical experiments.

To avoid being in a nonphysical behaviour, it is necessary to relate the numerical cohesion $C_{num}$ considered in the code to real values that can be observed in rocks. In the initial state of our model, each cohesive bond between any pair of contacting grains requires a certain amount of mechanical energy for breaking (breakage related both to its tensile and tangential stiffnesses, to its tensile and tangential strengths, and to its length $L_c$). To quantify the total amount of cohesion energy in the initial state of the fault (i.e. the energy that would be needed in order to break all the initial bonds), we normalize it with respect to a representative energy. This quantity corresponds to a surface energy of 62J/m² which was reported for the Chilhowee quartzite and considered as an upper limit for rock surface energy by (Friedman et al., 1972). This surface energy is applied on the whole external surface of all grains present in the simulation (a unit length is considered in the third dimension for any necessary purpose). This would correspond to 100% of cohesion, and the influence of this percentage is investigated in this paper (Figure 3 – c). Thus, a simulation case with a 20% as defined is to be interpreted in the sense that, in its initial state: (i) it has a complete cementation with only 20% of the reference surface energy, or (ii) it has the reference surface energy but has cemented bonds on only 20% of grains contours in average, or (iii) any combination of these two end-members. Detailed calculi are explained in the supporting information S4. In the following, we will use this X%, percentage of cohesion inside the sample, rather than the numerical cohesion which does not have any physical meaning.

## 3. Mechanical and physical gouge properties

### 3.1. Frictional strength and dilation

For both kinds of samples (dense and mid-dense), a number of simulations with various cohesion levels have been performed. (Figure 4 – a & b) provide typical curves of the measured coefficient of friction of the fault (i.e. resisting tangential force divided by the applied normal force) as a function of the horizontal displacement imposed to the upper wall. In all cases, the tangential force increases linearly until a maximum frictional strength $\mu_p$, demonstrating the maximal effort that

the loading system must provide to reorganise the gouge and accommodate imposed shearing. In the linear elastic part of the curves, dense and mid-dense samples have different initial slopes ($k_{dense} > k_{mid-dense}$). It should be noted that this stiffness is only related to the gouge layer itself, since no other compliance (related to the surrounding medium, for example) is considered in the simulations. For a given initial compacity, all simulations follow the same slope (different slope for dense and mid-dense samples), and adding more cohesion extends the mobilised friction before the peak.

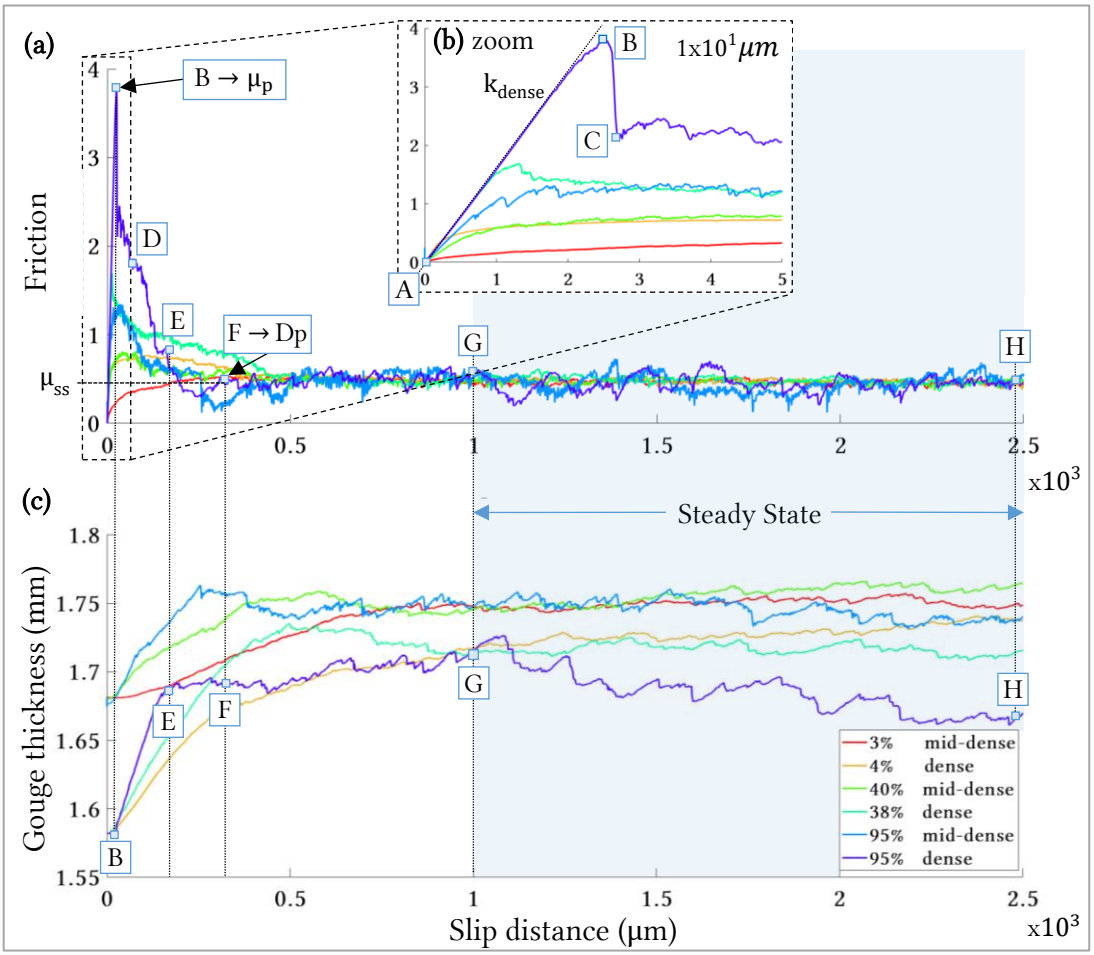


**Figure 4**. (a) Friction curve comparison between dense and mid-dense samples as a function of the slip distance (μm) – (b) Zoom in on the friction peak – (c) Gouge thickness variation (μm) as a function of the slip distance (μm) for dense and mid-dense sample. Letters corresponds to different steps in curves presented: [A] is the initial state before shearing and is identical in all cases. [B] is the friction peak location, [C] is the end of the first peak (only appears for

dense samples with a lot of cohesion), [F] is the observed end of the global friction peak, [G] is a common state for beginning of steady state and [H] is the end of simulation (results table in supporting information S5).

Depending on the percentage of porosity and on the cohesion level of each simulation, the peak strength may be sharp, short, and intense (dense and highly cohesive cases) or smooth, delayed and of moderate amplitude (mid-dense and moderately cohesive cases), (Figure 4 – a & b). After the peak, the apparent friction coefficient decreases in all cases towards a plateau, which corresponds to a steady state and does not evolve significantly any more until the end of the simulation. All steady-state friction values oscillate around the same macroscopic friction $\mu_{SS}$, (averaged from the beginning of the plateau until the end of the simulation). For all experiments, $\mu_{SS}$ is very close to 0.5 (ranging from 0.45 to 0.51). It is interesting to notice that this value is in agreement with other numerical studies (Rathbun et al., 2013), but lower than typical 3D experimental values (which are usually above 0.6). This discrepancy is related to the 2D character of the simulations (Frye & Marone, 2003).

As expected, the denser sample shows higher dilation rates than the mid-dense sample as the initial gouge is initially more compacted. When the steady state is reached, the average gouge thickness stays lower in the denser case (1.71 mm versus 1.75 mm in the mid-dense sample at steady state G (Figure 4 – c). It should be noted that these results are not in the range of small deformations, as the total slip displacement (2.5mm) is higher than the gouge thickness (≈1.75mm). The addition of a small cohesion (<10%), does not seem to disturb samples dilation, and results are similar to the case without cohesion for both kinds of samples: a progressive dilation until the steady-state "G", where gouge thickness is stabilized. The addition of an important cohesion (>10%) accelerates the typical dilation (Figure 4 – c). Beyond 80% of cohesion (blue curves - 95%), the peak of friction "B" corresponds to the beginning of the dilation, as some cohesive bonds need to be broken before any movement. The end of friction peak "F" coincides with the end of the major dilation phase. Although the steady state friction value "G" announces a friction stabilisation, it is also the beginning of a contracting behaviour. This delayed contractancy only appears for a very high level of cohesion and could be interpreted as the signature of a progressive comminution by decohesion of agglomerates within the sample.

(Figure 5 – a & b) gather the main characteristics of friction curves for the whole simulation campaign. Results obtained for a percentage of cohesion lower than 10% all lead to a similar

mechanical behaviour, both in terms of friction or dilatancy. However, when the cohesion level goes beyond the threshold of 10%, it has a noticeable effect on the friction peak, which increases with cohesion. When the cohesion level reaches values close to its maximum (100%), then the friction peak can reach 200% of $\mu_{SS}$ in the mid-dense case and almost 500% in the dense case (Figure 5 – a). It is very likely that such high values are related to the fact that the cohesion of the sample is very high while the confining stress is rather low (40 MPa), (Lade & Overton, 1989). Hence, they should not be interpreted as Coulomb-type (i.e. normal-stress-dependent) friction coefficients but rather as simple ratios between a normal and a tangential stress. As such, they cannot be directly generalized to situations where a different normal stress is applied on the fault.

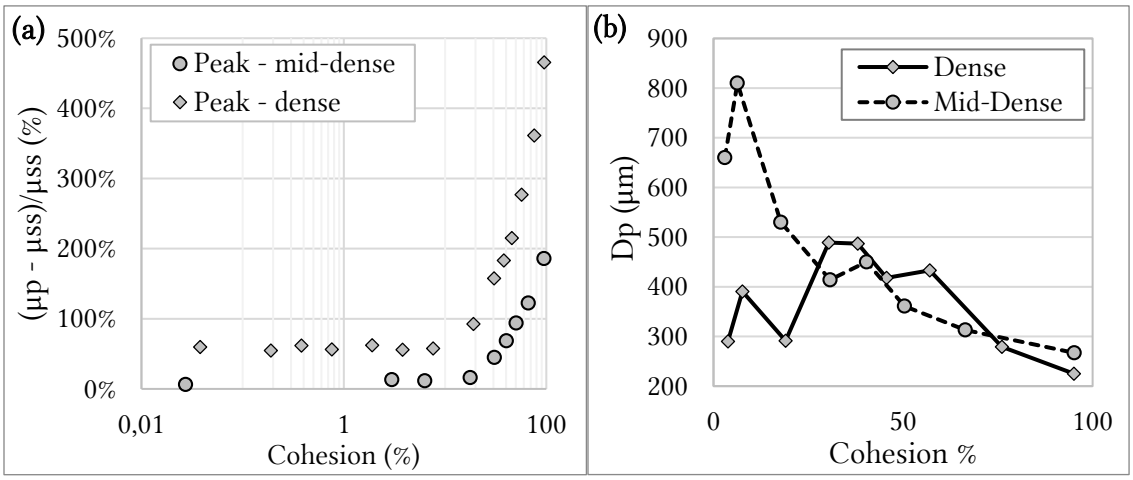


**Figure 5**. (a) Ratio between friction peak and steady-state friction as a function of the percentage of the cohesion in the model – dense and mid-dense samples - (b) Friction peak duration (μm) as a function of the percentage of cohesion within the gouge, for both dense and mid-dense samples.

In (Figure 5 – b), friction peak distance $D_p$ (not to be confused with the $D_c$ used in rate and state laws), is the distance between the peak of friction and the beginning of the steady state. $D_p$ value is derived from rupture energy calculation and can be related to the energy needed to weaken the fault until the steady-state of sliding (detailed are given in Section 0). The more cohesion we add within the gouge, the earlier the friction peak appears. For mid-dense samples, $D_p$ decreases with the increase of cohesion from 810 to 267 μm. Dense samples show a slight increase of the peak duration until a cohesion of 25% and then a decrease. We can highlight two main trends: with less than 25% of cohesion, mid-dense samples need a higher displacement to reach their steady-state

regime but with cohesion higher than 25%, $D_p$ is quite similar for both dense and mid-dense samples.

### 3.2. Gouge kinematics during sliding

Previous observations can be partly explained with the evolution of cohesive bonds between grains, which is represented as the increase of damage within the granular gouge. This damage is set to 0 when cohesive bonds are first established (all the bonds are intact) and may evolve until 1 if all these bonds reach the "broken" status (cf. Section 2.3). It is thus a relative damage with respect to an initial state. The representation of the relative damage gives a picture of the state of decohesion between grains and its location within the gouge. It also gives the opportunity to follow the formation of failure patterns (Riedel cracks, shear bands, etc.). Force chains and contact forces orientation are also key parameters in the understanding of the local and global gouge behaviour. Numerical experiments show that, for a given initial porosity, an increase of cohesion gives rise to three different modes of slip initiation (especially noticeable for dense samples). We can thus summarize these observations on kinematic ground by classifying the simulations in three main cases: mildly-cohesive (cohesion lower than ≈25%), cohesive (cohesion between ≈25 and ≈75%) and ultra-cohesive (cohesion larger than ≈75%). We can also note that the three regimes described below are considered as quasi-static regimes, the inertial number I remaining lower than 1e-3 (Pouliquen, 2011): microscopic rearrangements are much faster than macroscopic deformations.

#### 3.2.1. Mildly cohesive regime

The first case described is a mildly cohesive regime because the inter-particular cohesion introduced between grains is not sufficient to maintain cohesive bonds during shearing. (Figure 6 – b) reveals a very few number of tensile forces for $MD_3$ and $D_4$ (hereafter, $MD_n$ refers to mid-dense and $D_n$ refers to dense samples while n refers to the cohesion level), in accordance with the low percentage of cohesion in these samples. As soon as the upper rock wall is set into motion, almost all cohesive bonds break and only few of them resist until friction peak "$B_4$" (Figure 7).

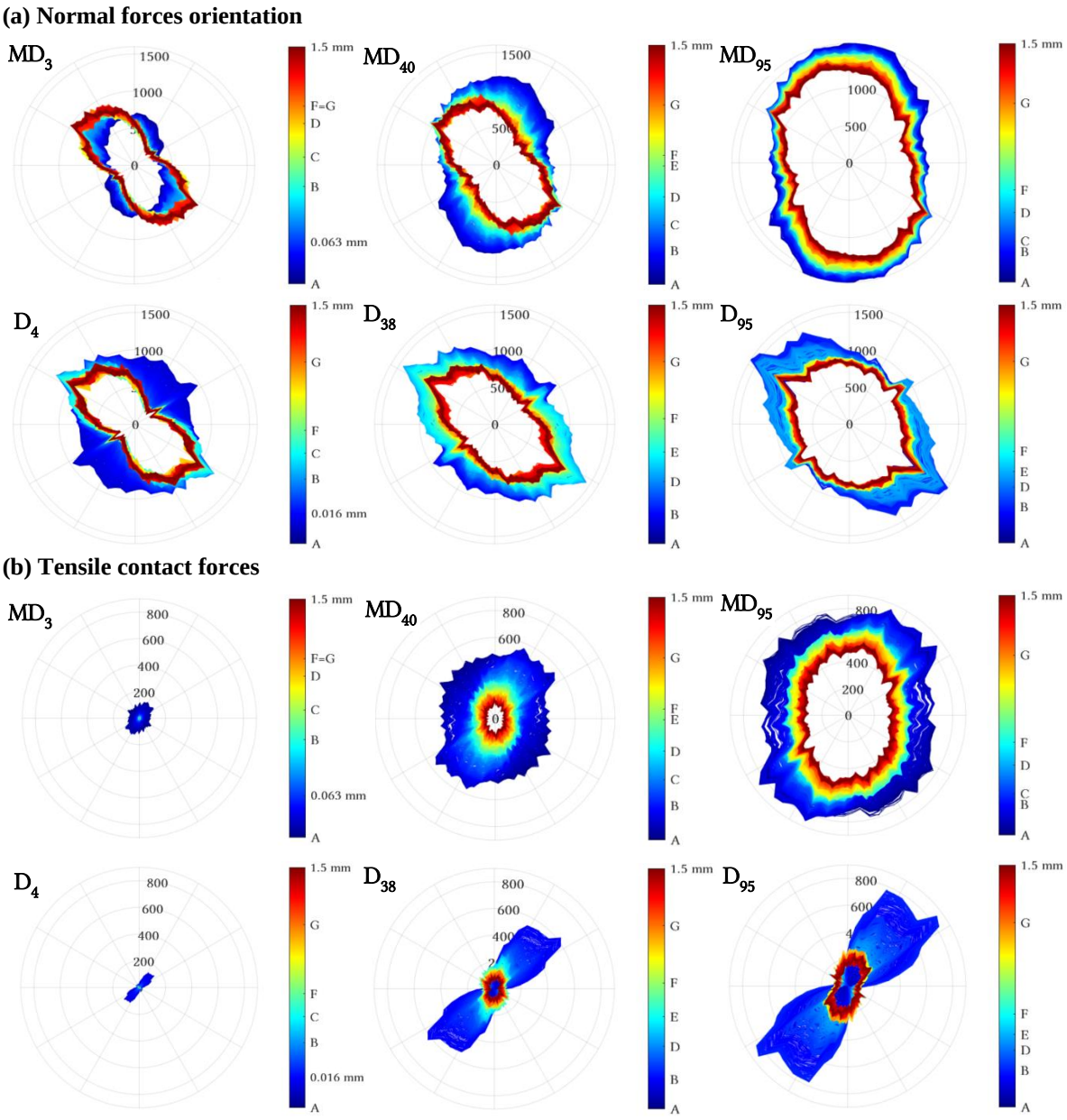


**Figure 6**. The graph provides the numbers of contacts with a normal vector oriented in a given direction (using polar diagrams where the Theta-axis is the orientation and the R-axis is the number of contacts), with a colour evolving during the different stages of each simulation – three regimes of cohesion: mildly cohesive [0-25%], cohesive [25-75%] and ultra-cohesive [75-100%] – from zero [A] to a slip distance of 1.5mm of the upper rock wall [H]. (a) Normal forces orientation (0-180°) within the gouge for mid-dense and dense sample – (b) Tensile contact forces orientation (0-180°) within the gouge for mid-dense and dense samples.

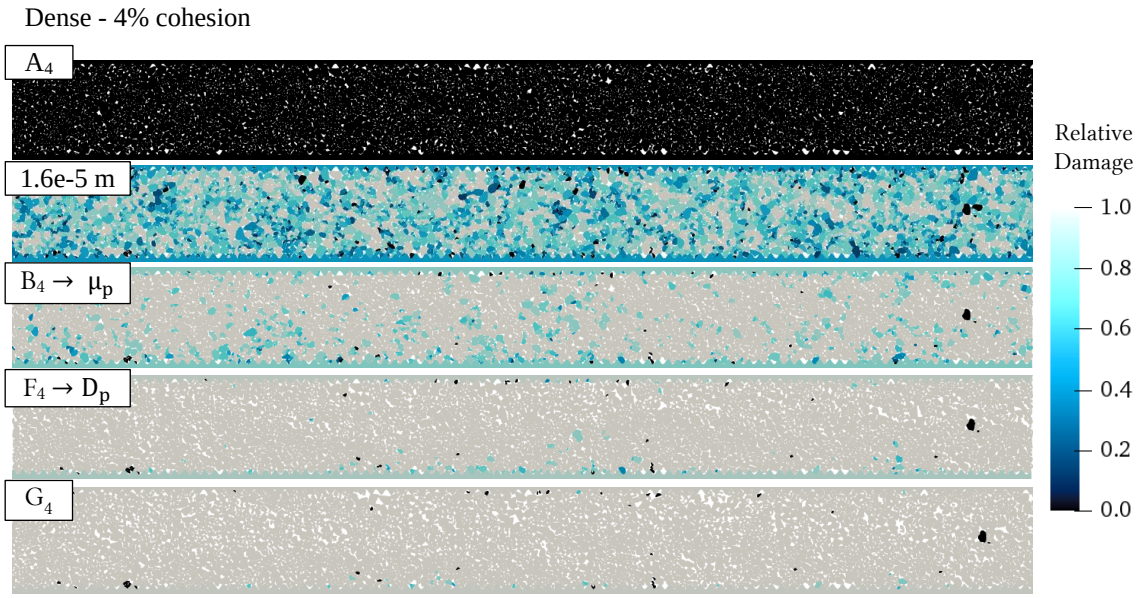


**Figure 7**. Relative damage snapshot for 4% of cohesion in the dense sample (entire granular gouge). Letters correspond to different steps in the curves presented in (Figure 4) ($A_4$: no damage and no slip distance, $G_4$: maximum damage and slip distance of 1mm).

At friction peak, this regime displays a preferential orientation for both normal contact forces and force chains inclined at 45° from the upper rock wall ($MD_3$ and $D_4$ in (Figure 6 – a) and $B_3$ and $B_4$ in (Figure 8). Similar orientation of force chains have been observed by (Morgan & Boettcher, 1999). The change of orientation of normal forces appears before friction peak, showing that the gouge already started to expand before reaching the peak. The evolution of the granular flow gives way to a Mohr-Coulomb contact law with inter-particle friction only. Once the gouge has dilated, grains can reorganize to allow shearing and the gouge tends towards a stationary state of sliding from the end of friction peak "$F_4$" to the end of simulation. The limited cohesion, the large dilatancy and the preferred orientation of force chains observed seem to confirm a typical granular Couette flow for the mildly cohesive regime [(GRD Midi, 2004) & (Da Cruz et al., 2005)].

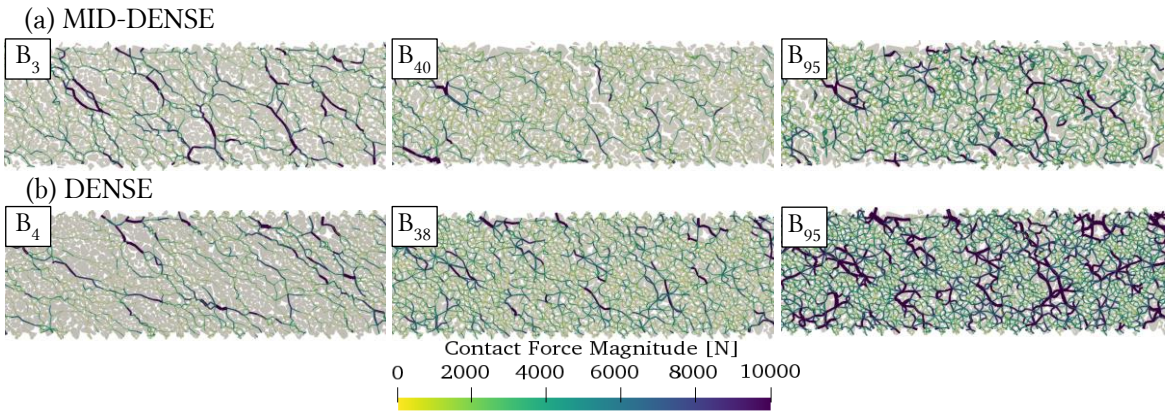


**Figure 8**. Snapshots of the force-chains networks at the friction peaks [B] for six chosen cases (0 to 1e4 N) – For 3-4, 40-38 and 95% of cohesion – In the pictures, only a quarter of the total gouge is displayed, and even if the global behaviour is similar to one quarter, force chains are not homogeneously distributed within the gouge after friction peak. (a) Mid-dense samples – (b) Dense samples

### 3.2.2. Cohesive regime

A second type of behaviour is presented (Figure 9), and corresponds to a cohesive granular regime (38 % of cohesion). Contrasting with the first case, this regime presents a clear augmentation of normal and tensile forces for both initial states "A" in dark blue and final states in red in (Figure 6 – a & b). Tensile contacts then reduce from friction peak "B" to the end of friction "F" with the breakage of cohesive links, but a lot of cohesive bonds remain active and play an important role in the gouge behaviour. In (Figure 7) presenting force chains, the orientation at 45° is not yet present at friction peak "$B_{40}$" and "$B_{38}$", because grains are just about to move and contacts between grains have not changed. Instead, there are smaller ramified force chains with a clear rising of intensity with cohesion. The denser sample gives a more homogenous distribution of force network (i.e.force chains) passing through almost all particles (Figure 8).

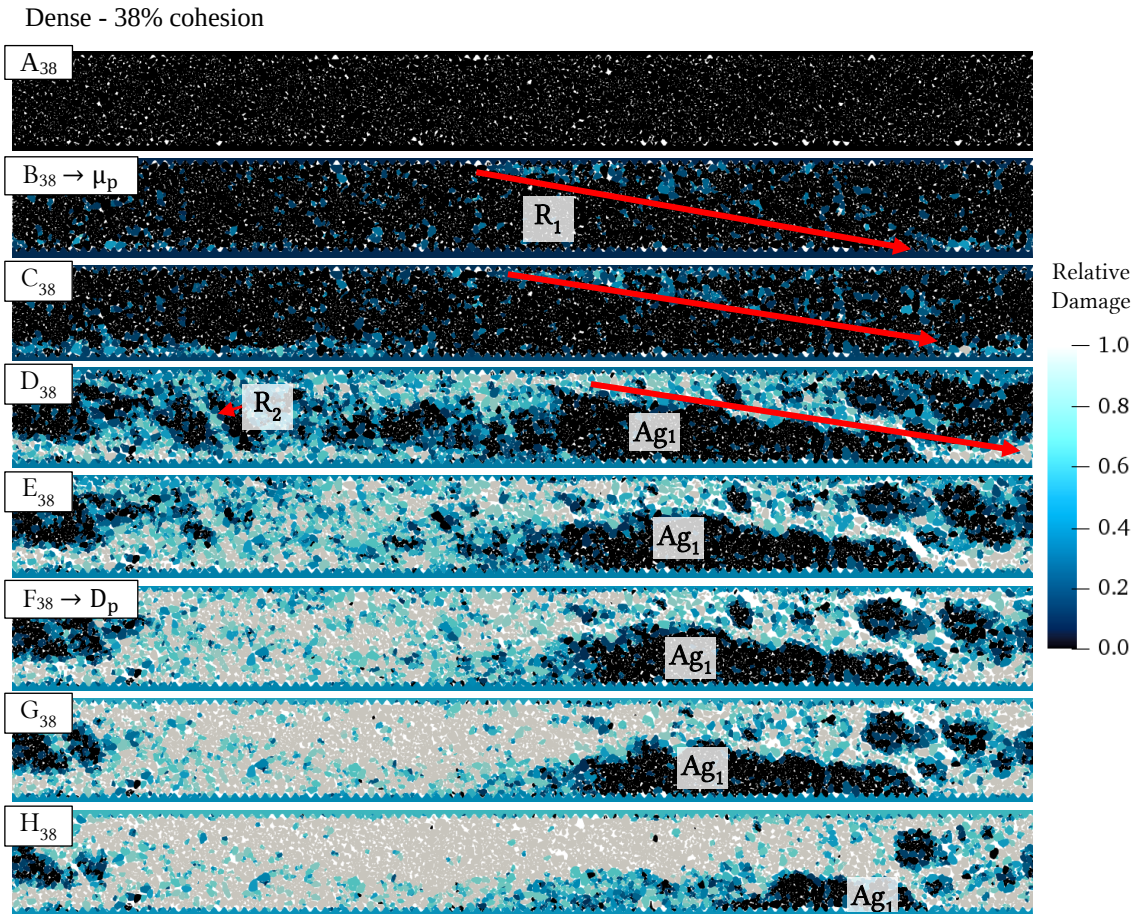


**Figure 9**. Relative damage snapshot for 38% of cohesion in the dense sample (entire granular gouge). Letters corresponds to different steps in the curves presented in (Figure 4). ($A_{38}$: no damage and no slip distance, $H_{38}$: slip distance of 2.5 mm). "Ag1" denotes a large agglomerate followed during its motion. The red arrow follows the low angle Riedel shear "R1" inside the gouge and "R2" is an example of high angle Riedel shear band.

Friction peak "$B_{38}$" is the starting point of a movement in the gouge with the highlighting of a preferential localisation of cohesive bonds rupture (red arrow in (Figure 9)) considered as the first Riedel deformation (Tchalenko, 1970). This rupture develops in the next stages of the simulation "$B_{38}$ to $H_{38}$" with a pattern similar to a Riedel crack R1 (oriented in the sheared direction, ~12° from the upper wall). The progression of the Riedel crack towards a shear band increases until the end of friction peak, where it is no longer detectable among the damage zone. The different Riedel geometries are associated with different shear deformation degree. R' shear bands are not visible in the numerical results, but we observe high angle Riedel shear "R2" or 'T' (for tensile crack).

From friction peak "$B_{38}$", damage evolution also highlights the presence of cohesive agglomerates formed by intact bonds within the gouge (ex: $Ag_1$), with a size decreasing with time. These clusters

can lead to rather inhomogeneous behaviours inside the granular gouge, changing the whole geometry and particle size distribution. Similar observations were made by [(Cho et al., 2008) & (Rognon et al., 2008)].

### 3.2.3. Ultra-cohesive regime

Increasing again the percentage of cohesion leads to an ultra-cohesive regime (95% cohesion) where most of the cohesive bonds stay intact during the entire simulation (Figure 10). Numbers of tensile forces and force chains magnitude are obviously higher than in previous regimes (Figure 6 & Figure 7).

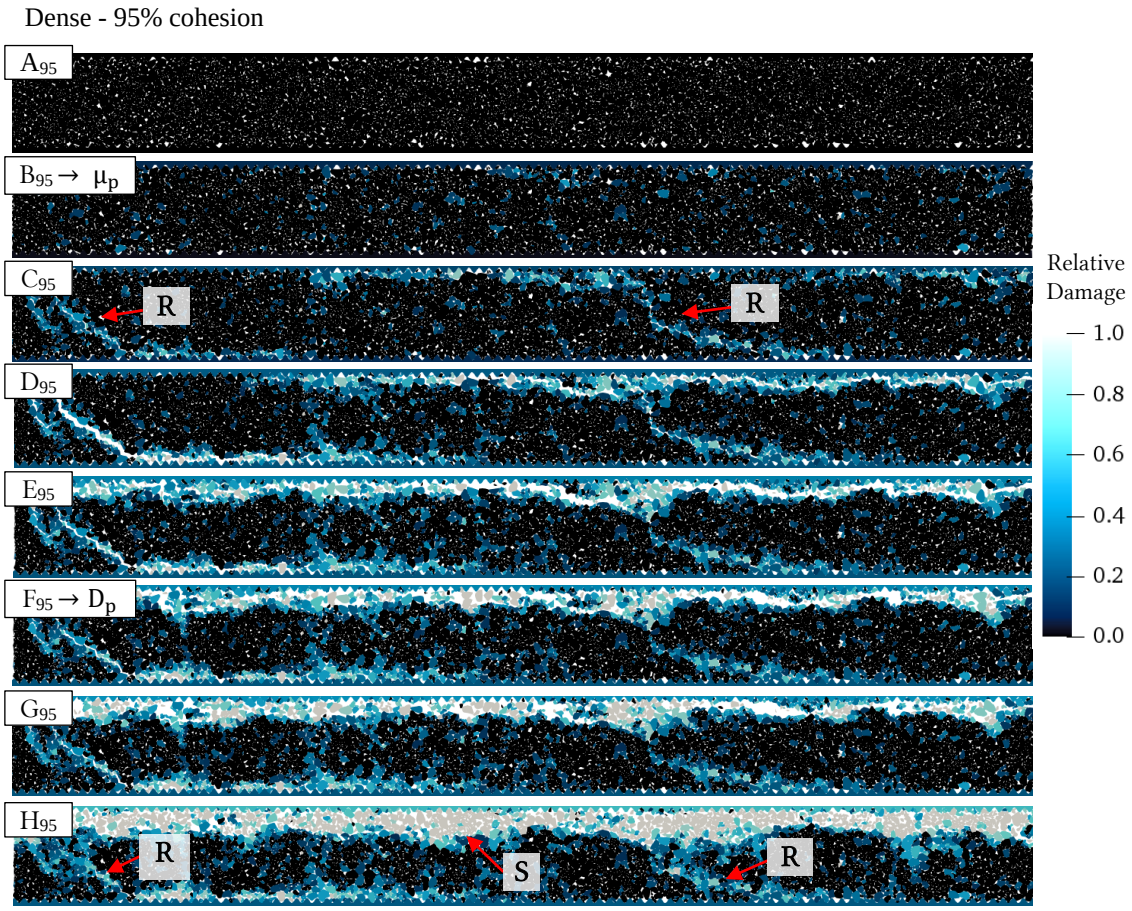


**Figure 10**. Relative damage snapshot for 95% of cohesion in the dense sample (entire granular gouge). Letters corresponds to different steps in the curves presented in (Figure 4). ($A_{95}$: no damage and no slip distance, $H_{95}$: slip distance of 2.5 mm). R represent the Riedel shear bands and S the horizontal shear localisation.

The highly cohesive rock enhances the formation of two Riedel cracks "R" at the second friction peak "$C_{95}$". The slip accumulation increases discrete faults and reduces the space between shear

bands (Katz et al., 2004). Thus, in the next steps, Riedel cracks progressively reduce in favour of an horizontal shear localisation "S" at the top of the granular gouge "$H_{95}$". Almost no deformation observed from "$E_{95}$" to "$H_{95}$" in the core gouge unless an increase of the thickness of the shear band "S".

In contrast to mildly cohesive cases where contacts take place between two particles, high cohesion contacts perform between packets of cohesive grains. The shearing localizes on the bottom or top part of the gouge letting the majority of particles behave as a single body. Some particles detached from these bands operate alone and create contacts between the cohesive band and rock walls where are passing all the efforts at the end of friction peak (Figure 11), defining clear geometrical asperities. A steady state is reached when enough of this tribological third body has been released to avoid any asperity contact and to produce a three-body sliding.

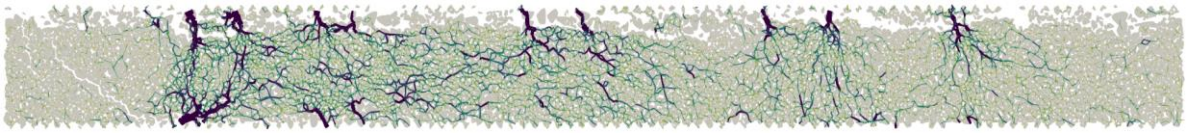

**Figure 11**. Snapshot of force-chains network at the end of friction peak [F] (from 0 to $1^{e}4$N) – 95% cohesion – dense.

Total gouge thickness first increases thanks to the emergence of aperities (i.e. grains emerging from cohesive bond breakage) and clusters of grains, forming inter-particle bridges, which releases gouge in the interface as the rupture is going on. The progressive breakage of cohesive agglomerates also explains the contractive response observed in (Figure 4 – c) in the second part of the simulation (from "$G_{95}$" to "$H_{95}$"). Results that can be compared to grain breakage at smaller scale [(Daouadji et al., 2001) & (Daouadji & Hicher, 2010)]. Normal forces orientation follow the same trend as the dilatancy: a first increase at the first step (due to inter-particle bridges formation) and a come back to the initial compacting state as the majority of cohesive contacts are still active (Figure 6) "$MD_{95}$" and "$D_{95}$".

As observed by (Rognon et al., 2008), we also notice for these highly dense and cohesive samples, a fluid-like top layer and a solid-like bottom layer (with a thickness increasing with the cohesive bonds).

### 3.2.4. Comparison with mid-dense sample

Mid-dense samples present a higher relative damage. The less compacted initial state allows easier grains reorganisations (Figure 12). One high angle Riedel shear band "R2" in the 40% case, and two high angle Riedel cracks "R2" in the 95%, are followed by an horizontal shear localisation "S" at the bottom of the granular gouge. Whatever the cohesion level, the initial preferred orientation of normal forces "A" changes between dense and mid-dense samples. Dense samples give an homogeneous repartition of normal orientations and mid-dense samples present normal forces mostly oriented perpendicularly to rock walls, dark blue zones in (Figure 6 – a).

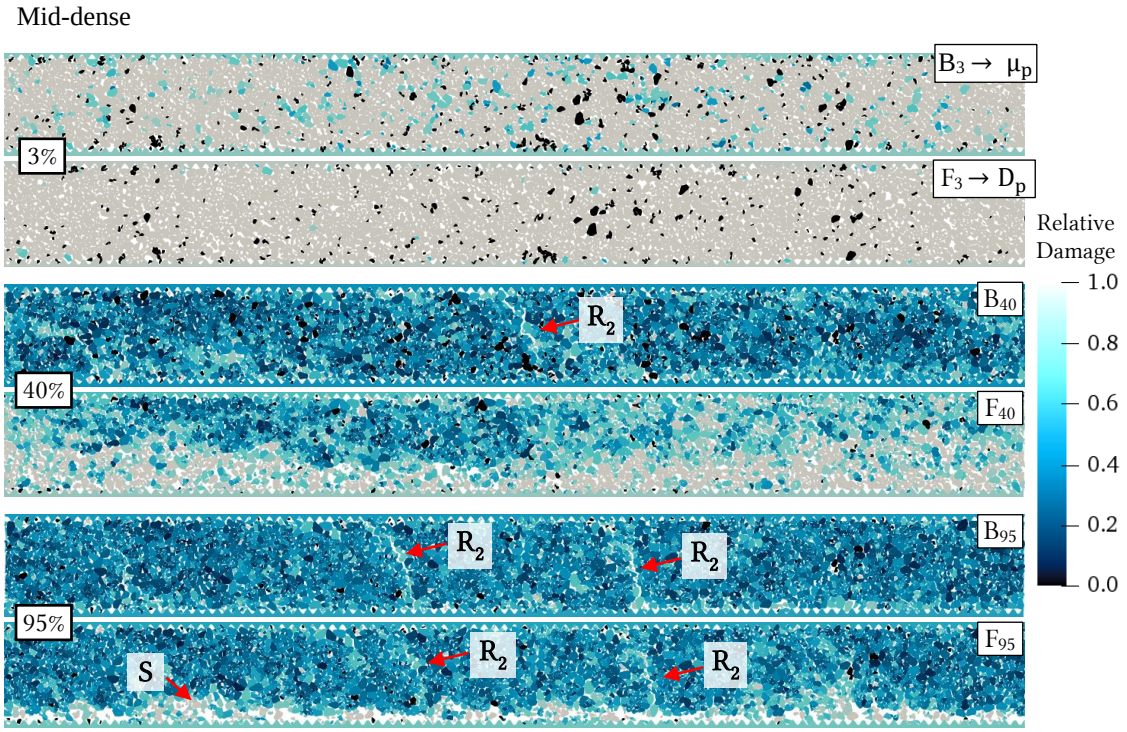


**Figure 12**. Relative damage snapshots for mid-dense sample (entire granular gouge). For both peak [B] and end of friction peak [F]. Letters corresponds to different steps in the curves presented in Figure 4. $R_2$ represent high angle Riedel shear bands and S the horizontal shear localisation.

## 3.3. Decomposition of sliding friction

Simulation results show that a modification of the initial density (i.e. porosity), or of the cementation within the sample could induce a change in slip mechanisms. But they are also a way to give a different point of view on how to link rupture with gouge properties. In order to isolate the main mechanisms acting on fracture processes, we propose a new partition of the total macroscopic friction generated during the shearing of a granular gouge. Based on the physical

content of the numerical model, three factors are identified as playing a role on total mobilised friction: (i) the dilation of the gouge (deformation in the direction perpendicular to the sliding), (ii) the decohesion coming from the breakage of cohesive links, and (iii) the friction generated by sliding contact interactions. These contributions are calculated thanks to global potential energy recovered at each time step, from the data set presented in previous sections and computations details presented in Supporting Information S6.

(Figure 13 – a) shows an example of the total friction (black curve) and its different contributions as a function of the slip distance for a dense sample with 30% cohesion. The green curve is the sum of the Coulomb and elastic contributions, the dilatancy contribution appears in red and the decohesion contribution in blue. We propose to reproduce these slip-friction curves (derived from energy contributions) with simplified models (in dark in (Figure 13 – b, c, d & e)) by means of global parameters laws. These parameters are chosen and adjusted to picture the global trend of friction contributions.

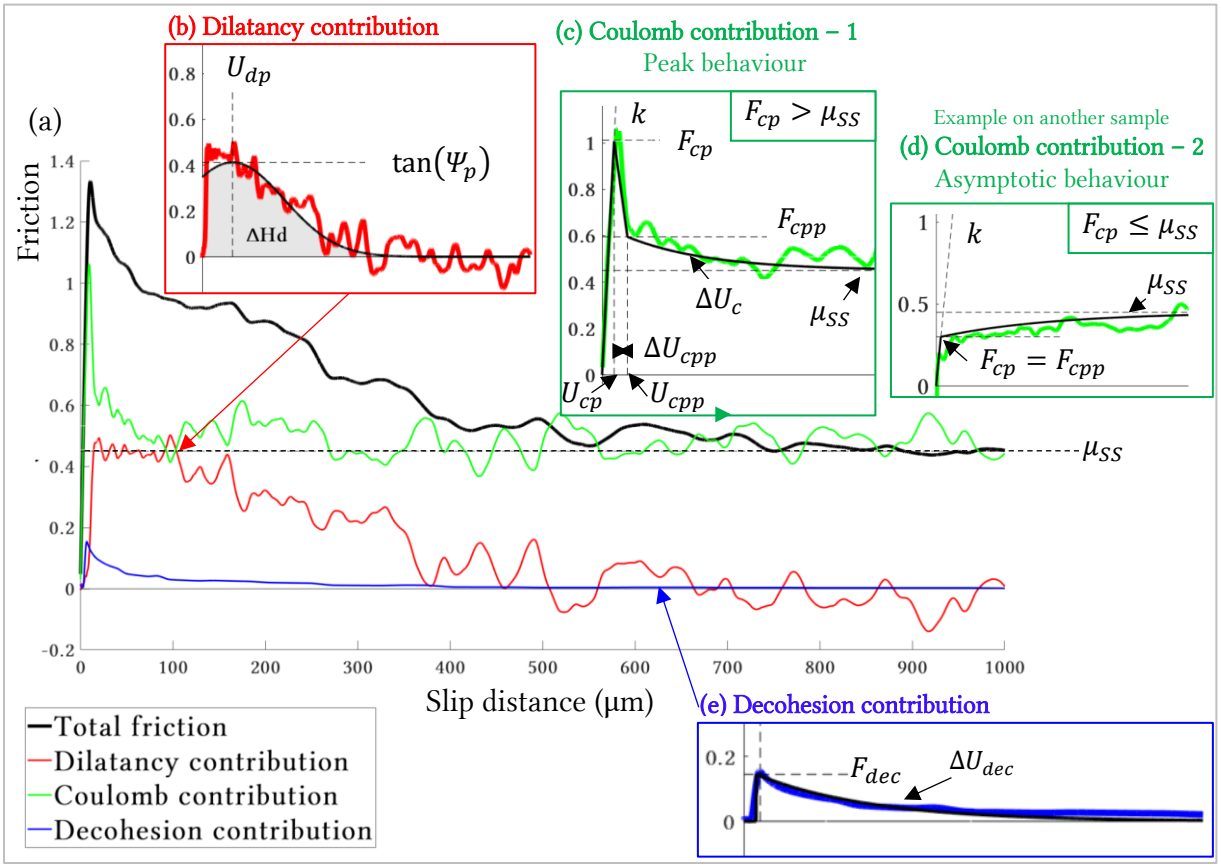


**Figure 13**. (a) Friction-slip curve with different contributions (dilatancy in red, Coulomb in green and decohesion in blue) - dense sample – 30% of cohesion – The black curve is the sum of all contributions. (b) Zoom in on dilatancy

contribution, simulation data in red and simplified model in dark. (c) Zoom in on the Coulomb contribution, simulation data in green and simplified model in dark, the 30% dense case corresponds to the first type of Coulomb model. (d) Example of the second type of Coulomb model, zoom in on Coulomb contribution of the 30% mid-dense case. (e) Zoom in on the decohesion contribution for the 30% dense sample.

The dilatancy friction evolution can be illustrated by means of three parameters, $\Psi_p$ the maximum dilatancy angle (Rowe, 1962), $U_{dp}$ the sliding distance corresponding to the maximum dilatancy, and $\Delta H_d$, the gain in gouge thickness at the end of the dilatancy phase (Figure 13 – b). These parameters are introduced in a Gaussian distribution with a maximum dilatancy friction of $\tan(\Psi_p)$ and a squared exponential decrease as a function of slip:

$$F_{dil}(U) = tan(\Psi_p) \cdot e^{-log2\left(\frac{U-U_{dp}}{U_{d_{half}}-U_{dp}}\right)^2} \quad (3.3.1)$$

U is the current displacement of the upper rock wall and $U_{dhalf}$ is the distance between $U_{d_p}$ and the slip distance for a half reduced dilatancy-related friction. This last parameter is determined by solving numerically:

$$\frac{U_{dhalf}-U_{dp}}{2} \cdot \tan(\Psi_p) \cdot \sqrt{\frac{\pi}{log2}} \cdot \left(1 + erf\left(\frac{U_{dhalf}}{U_{dhalf}-U_{dp}} \cdot \sqrt{log2}\right)\right) = \Delta H_d \quad (3.3.2)$$

The Coulomb contribution is more complex to model because two different behaviours are observed. The first one is a peak behaviour where the Coulomb friction peak $F_{cp}$ is higher than $\mu_{SS}$ (Figure 13 – c). It exhibits a first linear elastic part characterized by a stiffness $k$ (gouge layer stiffness) from 0 to $F_{cp}$. Then friction decreases linearly until a post-peak value called $F_{cpp}$. Coulomb contribution to friction finally diminishes exponentially until $\mu_{SS}$, taken as 0.45 to simplify the model.

$$For\ U \leq U_{cp} \qquad F_c(U) = kU \quad (3.3.3)$$

$$For\ U_{cp} \leq U \leq U_{cpp} \qquad F_c(U) = \frac{(F_{cpp}-F_{cp})}{\Delta U_{cpp}}(U-U_{cp}) + F_{cp} \quad (3.3.4)$$

$$For\ U_{cpp} \leq U \qquad F_c(U) = \mu_{SS} + (F_{cpp}-\mu_{SS}) \cdot e^{-\frac{U-U_{cpp}}{\Delta U_c}} \quad (3.3.5)$$

With $\Delta U_c$ a characteristic distance of the exponential decay, $U_{cp} = \frac{F_{cp}}{k}$ , $\Delta U_{cpp}$ the slip distance between $U_{cp}$ and $U_{cpp}$ and $U_{cpp} = U_{cp} + \Delta U_{cpp}$.

The second type with $F_{cp} \leq \mu_{SS}$ displays the succession of an elastic part from 0 to $F_{cp}$ followed by an asymptotic exponential behaviour until $\mu_{SS}$ (Figure 13 – d). This case is especially observed in mid-dense samples or for mildly cohesive regimes:

$$For\ U \leq U_{cp} \qquad F_c(U) = kU \tag{3.3.6}$$

$$For\ U_{cp} \leq U \qquad F_c(U) = \mu_{SS} + \left(F_{cp} - \mu_{SS}\right) \cdot e^{-\frac{U - U_{cp}}{\Delta U_c}} \tag{3.3.7}$$

With $F_{cpp} = F_{cp}$ and $U_{cp} = \frac{F_{cp}}{k}$

The last contribution is the decohesion, characterized by an absence of contribution during elastic loading, and a maximum friction peak $F_{dec}$ followed by an exponential decrease until 0 (Figure 13 – e):

$$For\ U \leq U_{dec} \qquad F_{dec}(U) = 0 \tag{3.3.8}$$

$$For\ U_{dec} \leq U \qquad F_{dec}(U) = F_{dec} \cdot e^{-\frac{U - U_{dec}}{\Delta U_{dec}}} \tag{3.3.9}$$

With $\Delta U_{dec}$, a characteristic distance of the exponential decay, and $\Delta U_{dec} = \Delta U_c$.

(Figure 14) presents the proposed evolution for each parameter as a function of the cohesion after fitting on all the simulation data, accounting for the three distinct regimes described in Section 3.2. The objective of this simplified model is not to reproduce the exact location of dilatancy friction peak, but to model a global and consistent shape evolution from one case to another (Figure 14 – a, b & c). Pushing up cohesion increases Coulomb friction peak and post peak friction that follow a linear law (Figure 14 – d), with a characteristic distance $\Delta U_c$ remaining almost constant for dense samples, and decreasing for mid-dense samples (Figure 14 – e). For decohesion contribution, $F_{dec}$ evolves as a rising linear law from 0 to 100% cohesion (Figure 14 – f) in accordance with previous results (Section 3.2). Taking into account every friction contribution, this new model gives a simplified representation of the final friction coefficient as a function of the initial percentage of cohesion. The proposed functional expressions and parameters evolutions of this model remain theoretical and might be modified or improved based on future findings, but allow to enrich slip-

weakening laws by proposing a more general model that could be implemented in dynamic rupture modelling. More details are presented in the supporting information S7.

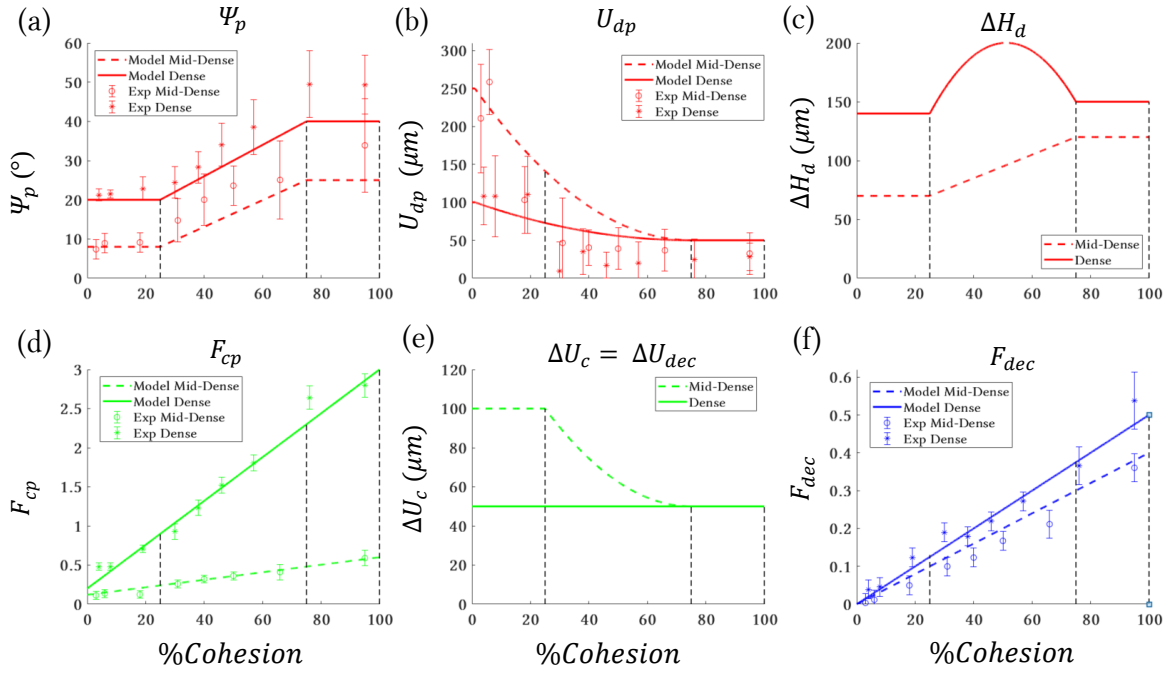


**Figure 14**. Model of friction laws presenting the 7 parameters taken into account in the simplified models. It can be noted that k, $\mu_{SS}$, and $\Delta U_{cpp}$ do not depend on cohesion and are taken as constant. (a) Maximum dilatancy angle Ψp. (b) Slip distance corresponding to the maximum dilatancy $U_{dp}$. (c) Gain in gouge thickness at the end of the dilatancy phase $\Delta H_d$. (d) Peak friction at the end of the elastic phase $F_{cp}$ and post peak friction $F_{cpp}$. (e) Characteristic distance of the exponential decay $\Delta U_c$. (f) Maximum friction induced by decohesion $F_{dec}$. Dots are experimental data derived from DEM modelling. They may be not aligned with numerical modelling as some peak values are difficult to identify on raw data and the error can be important. $\Delta H_d$and $\Delta U_c$ don't have experimental data, as they are completely created for the model.

## 4. Discussion: from gouge properties to rheological behaviour

### 4.1. Breakdown energy and slip weakening

#### 4.1.1. Local Breakdown energy

Throughout an earthquake, energy is dissipated during fault sliding by the means of different mechanisms. (Figure 15 – a) schematises the total energy budget $\Delta W$ of this rupture propagation based on classical slip weakening models. Although $E_H$ represents an important part of the total energy budget it does not strongly influence rupture processes. (Kanamori & Rivera, 2006)

differentiate the simple rupture energy from the fracture energy gathering material laws but also all delayed weakening processes such as melting (Giulio Di Toro et al., 2006) or fluid pressurization (J. R. Rice, 2006). However, these mechanisms will occur in a second time after the end of the first slip weakening phase according the definition of [(Kanamori & Heaton, 2000) & (Scholz, 2002)], generally because of thermal effects.

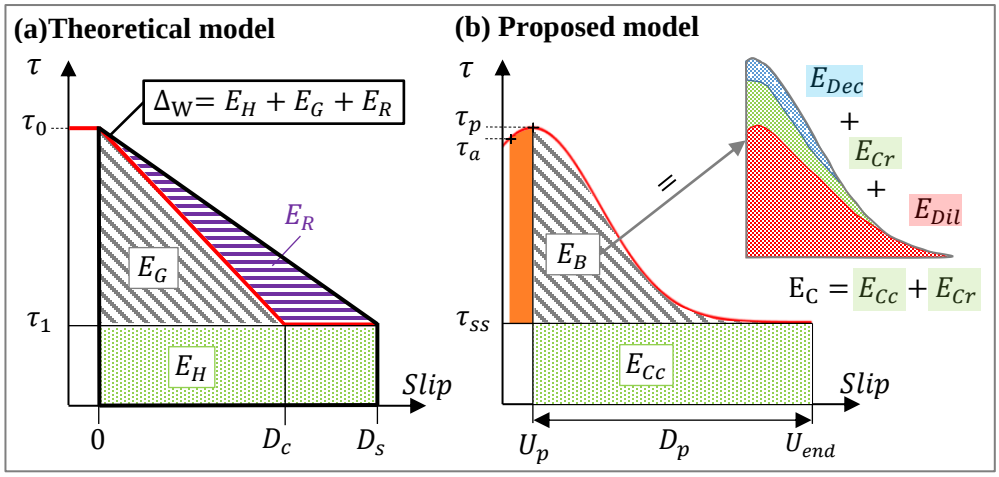


**Figure 15**. (a) Theoretical model of energy budget with $\Delta W$ as the sum of a fracture energy $E_G$, a radiated energy $E_R$ (propagating by the mean of elastic waves) and a frictional energy $E_H$ (dissipated within the slip zone). $\tau_0$ is the initial static shear stress, $\tau_1$ the dynamic shear stress, $D_c$ is the slip weakening distance and $D_s$ the end of slip displacement. This energy budget model is based on linear slip weakening theory - (b) Proposed model (function shape strongly varies depending on cohesion and initial porosity), with decomposition of the breakdown energy $E_B$. $E_B$ gathers a dilatancy energy $E_{Dil}$ linked to sample dilation (mechanical energy), a Decohesion energy $E_{Dec}$ coming from the breakage of cohesive links (surface creation energy) and $E_{Cr}$ a part of Coulomb energy $E_C$. $\tau_a$ is the initial static shear stress, $\tau_p$ is the maximum shear stress, $\tau_{ss}$ is the steady-state shear stress, or dynamic shear stress. $D_p$ is the friction peak duration. Coulomb energy $E_{Cr}$ collects all the Coulomb energy that is not considered in the constant part $E_{Cc} = \tau_{ss} * D_p$. Note that in the sketch, $E_B$ and $E_{Cc}$ are in Joule and not in J/m² as in the equation.

In this model, the focus is made on non-radiated energy and on non-heat production, and more precisely on post-peak rupture energy called $E_B$ $(J/m^2)$ for Breakdown Energy (i.e. the deformation potential energy that has to be spent to weaken the fault (Figure 15 – b). It can be calculated from numerical experiments carried out in the previous part as the area under the friction-slip curve, corrected by subtracting the steady-state friction:

$$\mathrm{E_B} = \int_{U_p}^{U_{end}} \frac{[\mu\,(U) - \mu_{\mathrm{ss}}\,] * \sigma_N}{S_{gouge}}\, d_U \qquad (4.1.1)$$

With $\mu\,(U)$ the current macroscopic friction, $U_p$ the displacement at friction peak, $U_{end}$ the displacement at the end of friction peak and $U$ the current slip distance.

According to previous assumptions and models presented above in (Figure 15 – b), the total Breakdown energy results in a new decomposition of the well-known Fracture energy $E_G$. $E_B$ gathers a dilatancy energy $E_{Dil}$ linked to sample dilation (mechanical energy), a Decohesion energy $E_{Dec}$ coming from the breakage of cohesive links (surface creation energy) and $E_{Cr}$ a part of Coulomb energy $E_C$. The remaining Coulomb energy $E_{Cr}$ collects all the Coulomb energy that is not considered in the constant part $E_{Cc} = \tau_{ss} * D_p$. Considering that the $E_{Cc}$ is similar to the definition of the $E_H$ part of energy budget, $E_{Cr}$ could be compared to an excess (or a deficit, if negative) of heat creation with respect to the steady-state rate of such heat creation.

(Figure 16) displays the evolution of all the contributed energies composing $\mathrm{E_B}$, as a function of the percentage of cohesion, for both dense and mid-dense samples, and based on previous simplified models. Regarding the previous Section 3, the evolution of $\mathrm{E_B}$ is consistent with the three distinct regimes. The mildly cohesive regime [0-25%] presents a low and constant energy release (higher energy for denser samples), the cohesive regime [25-75%] an energy increasing as a function of cohesion and the ultra-cohesive regime [75-100%] a constant energy released higher than the first regime. These curves confirm that both the percentage of cohesion and the initial porosity play a role in the mechanical behaviour observed. $\mathrm{E_B}$ also varies between 1 MJ/m² and 10 MJ/m², which is consistent with values of $\mathrm{E_G}$ presented by (Abercrombie & Rice, 2005) for a total displacement between 1 and 10mm.

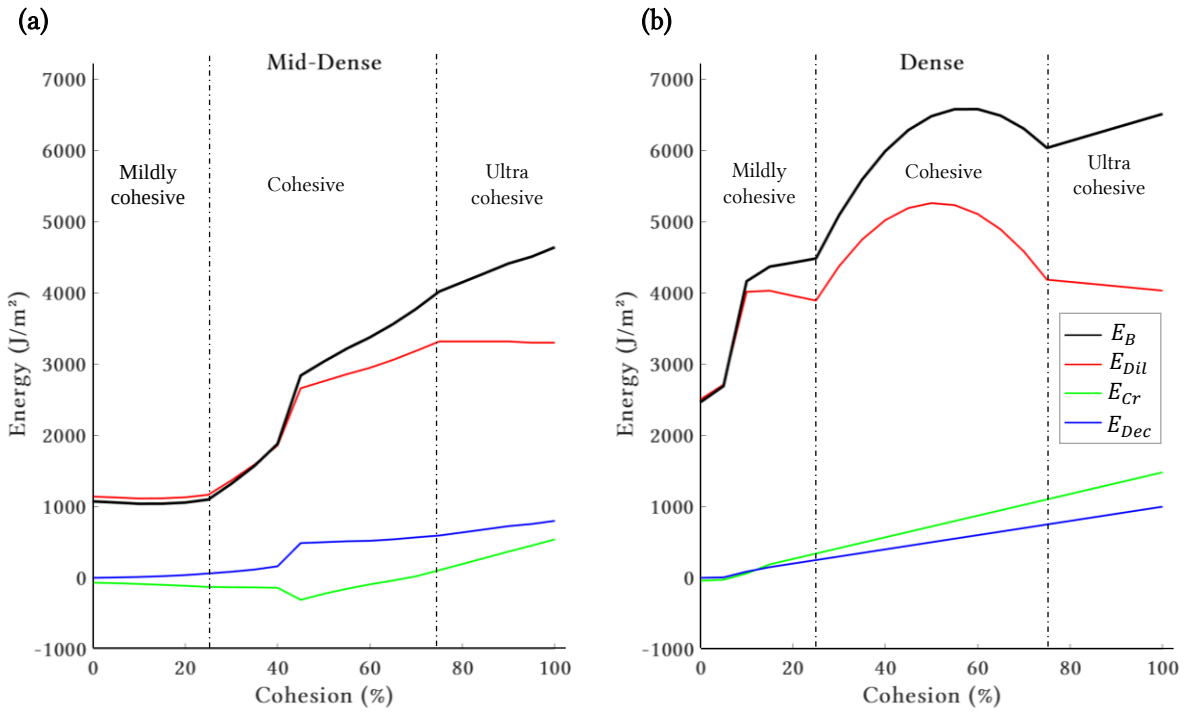


**Figure 16**. Breakdown energy (J/m²) coming from the different contributions as a function of the percentage of cohesion within the gouge. (a) Mid-dense samples (b) Dense samples. $E_B$ (in black) gathers a dilatancy energy $E_{Dil}$ (in red) linked to sample dilation (mechanical energy), a Decohesion energy $E_{Dec}$ (in blue) coming from the breakage of cohesive links (surface creation energy) and $E_{Cr}$ (in green), a part of Coulomb energy $E_C$.

Comparing the scale of each energy, dilation appears to be the most influent factor, while the other energies do not exceed 2 kJ/m². The dilatancy energy both increases with the percentage of cohesion and the initial density of the sample. This is consistent with previous results showing higher dilation for denser sample (Figure 4 – c). Decohesion energy increases with the percentage of cohesion and is almost similar for both kinds of samples. Indeed, the energy needed to break a cohesive link does not depend on the initial state of porosity, but rather on the contact length and the percentage of cohesion initiated. The Coulomb energy presents a special behaviour with a zero contribution for first regime and a small increasing contribution for the other regimes (Figure 16 – a & b). An interesting point is that only this term may lead to heat creation in the system (in addition or subtraction of the steady state friction), since dilation energy is nothing but a mechanical work and decohesion energy is related to surface creation. The constant part of Coulomb energy $E_{C_c}$ (not taking into account in $E_B$) appears to be twenty times higher than $E_B$ for the total slip considered here. This high difference explains why (Chester et al., 2005) consider that the Fracture energy is

negligeable in comparison to the other energies presented in the theoretical energy budget (Figure 15 – a). However, the knowledge of $E_B$ is crucial for the determination of the onset of sliding.

#### 4.1.2. Comparison to existing slip weakening modelling

Our model takes place within the framework of "Small Earthquakes" defined by (Kanamori & Heaton, 2000) and in the early beginning of a fracture process (without the "delayed" weakening phenomena or heat related phenomena). The (**Figure 17**) presents the proposed simplified models obtained for dense and mid-dense samples, with the three contributions described above.

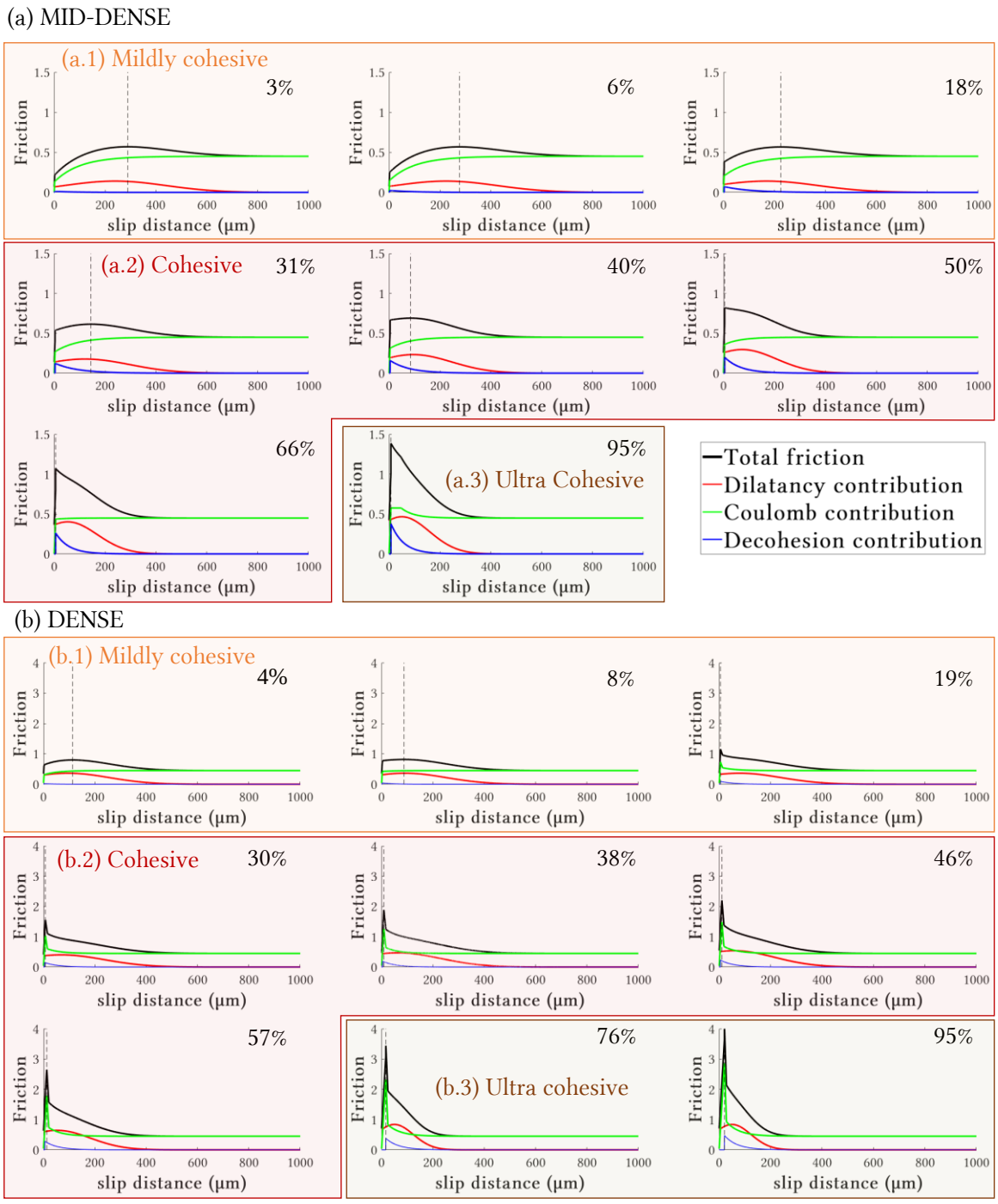


**Figure 17**. Proposed simplified models - Evolution of friction contributions as a function of the initial cohesion – (a) Mid-dense sample – (a.1) mildly cohesive regimes, where the observed pre-peak phase is important - (a.2) Cohesive regimes with a diminution of the pre-peak phase with the increase of cohesion - (a.3) Ultra cohesive regimes with no pre-pic phase. (b) Dense sample - (b.1) mildly cohesive regimes with a diminution of the pre-peak phase with the

increase of cohesion – (b.2) Cohesive regimes with a negligible pre-peak phase but an important influence of friction peak – (b.3) Ultra cohesive regimes with almost not pre-peak phase and an very high Coulomb friction peak.

Even though they take place in a specific range of experiments (constant imposed pressure, high slip velocity and absence of water), our results raise the question of the slip weakening shape and energy release. It appears that only mid-dense samples can be easily modelled with the classical linear form as presented in (Figure 15 – a). Dense samples display a bilinear decreasing shape that can be compared to a model proposed by (Abercrombie & Rice, 2005).

Exponential weakening models are used by (Sone & Shimamoto, 2009) in their high-velocity friction experiments. Although their results cannot be directly compared with the ones presented here, we can analyze the method used to model friction. The friction curve described by an exponential fit is consistent with some of our mid-dense samples but not for dense samples. The reason may be that in dense or ultra-cohesive samples, the dilatancy friction peak appears after the main friction peak, and a simple exponential decrease considers that all the physics is acting in the same time, which is not the case for very cohesive material (Figure 17 – a.3 & b.3). Saying differently, dilatancy friction peak may drive the whole fracture mechanisms for mildly cohesive and part of cohesive regimes. However, very dense and cohesive samples are first driven by frictional contacts and then by dilation.

$E_G$ both depends on material properties and rupture processes, and a noisy stress-slip curve leads to difficult interpretation of the different energy contributions. The partition of friction curves isolates the different contributions to easily highlight which phenomenon is happening for each physical behaviour observed. The curve shape seems to be important to be well modelled, as it gives information of when and where most of the energy is released and allows to have a direct link between rheology and physics. Simplified models proposed are pretty convincing about the final shape and could be adapted to a variable imposed stress and velocity, if properly fed with additional simulations.

### 4.2. Link between rheological behaviour and fault zone structure

"*To describe a fault zone, we must address two main problems: (a) the definition of the geometrical and mechanical properties of a fault zone and (b) the understanding of the spatial and temporal scale dependence of relevant physical processes*" (J. Rice & Cocco, 2005). Comparing gouge properties, shear bands and breakdown energy, we evaluate the link between gouge properties and

fracture mechanisms. In previous Sections, three main states of cementation (maturity of the gouge) represented by cohesive regimes were highlighted to describe gouge behaviour. Our results demonstrate that both gouge cohesion and gouge porosity play a role in the rupture process.

(Faulkner et al., 2008) added that the percentage of ductility within the fault gouge influences fracturing processes. The mildly cohesive regime shows a ductile trend, with a progressive particle reorganisation, and no localized shear is observed in (Figure 7). It should be noted that, in the present context, "ductility" is to be understood in the sense of granular mechanics but does not involves visco-plactic phenomenon. A low percentage of cohesion does not affect the granular medium (all cohesive bonds break in the beginning of the shearing) and the energy needed by the system remains relatively small compared to the two other regimes (1e3 J/m² for mid-dense case and around 3e3 J/m² for dense case) in (Figure 16 – a & b). For this Couette shearing, a high dilatancy rate begins in the pre-peak phase, giving an important "pre-peak" dilatancy energy (Figure 17 – a.1 & b.1). However, Coulomb and decohesion energies are negligible compared to dilatancy energy, both in pre-pic or post-peak phases.

An increase of cohesion level (cohesive regimes) allows the formation of particles agglomerates (Figure 9 & Figure 12) rising up the total shear resistance (Figure 4 – a). But these cohesive packages also modify the particle size distribution within the gouge, which is well-known to act on shear bands formation in addition to the initial density of the sample (Marone & Scholz, 1989). This second regime is viewed as transitional, and similar to semi-brittle behaviour. For dense samples, dilatancy is only acting when friction peak is reached (Section 3 and (Figure 17 – b)), giving a higher post-peak dilatancy energy than for mildly cohesive regime. We should emphasis that shear localisations appears with the peak of dilation. For mid-dense samples, an early friction peak occurrence results in a higher dilatancy energy, but dilation both occurs before and after friction peak (Section 3 and (Figure 17 – b)).

For ultra-cohesive regime, two main elements point towards a brittle behaviour. The first information comes from the observation of Riedel shear bands formation (Figure 10): even after friction peak, the structure observed is almost entirely cohesive and Riedel bands are enhanced, giving birth to shear localization. These Riedel bands appear with the beginning of dilatancy and shear localization at dilatancy friction peak (Figure 10 & Figure 17). The quasi-absence of pre-peak phase on friction-slip curves is the second element that shift towards a brittle behaviour of the

fault gouge (Figure 17 – a.3 & b.3). The pre-peak phase stops at the end of the elastic phase and the decohesion and dilatancy peaks are observed later in the post-peak phase. A denser material will present a more localized and brittle mechanical behaviour than a loose sample. Indeed, Riedel shear bands creation are directly linked to the importance of the dilation phase, which in turn depends on the initial porosity of the sample. These cracks are more visible in a sample with brittle behaviour (two T cracks opposed to one for semi brittle behaviour), and can be compared to T-fracture (Katz et al., 2004). These cracks also emerge for a higher slip displacement, they are related to the dilation phase observed later on in ultra-cohesive regimes. Besides, tensile contact orientation gives informations about the type of Riedel bands observed (Figure 6 – b, Figure 10 & Figure 12).

The importance of the pre-peak energy on fracture mechanisms seems poorly documented in the literature. Looking at our mildly cohesive models, pre-peak energy (i.e. energy derived from the first microcrackings developed before the macroscopic shear fault) results in being as important as the Breakdown energy calculated. (Ohnaka, 2003) reinterpreted the shear rupture energy $E_G$ as the sum of a fracture energy $G_{c1}$ (i.e. pre-peak energy) and of the post- peak energy $G_{c2}$ required for the breakdown from peak strength to residual friction. That study recalls that, without $G_{c1}$, intact rock cannot fail, so this pre-peak energy cannot be neglected. What we can add is that this pre-peak energy can be neglected in very cohesive and dense regimes, where the majority of the energy is released after friction peak. However, it seems to be important to include the pre-peak energy in case of poorly cohesive materials. To include or not this pre-peak energy in the total energy budget in thus questioned, and also strongly depends on the initial stress applied on the fault before arrival of the sliding front. However, one can assume that this energy participates actively to shear rupture processes.

## 5. Conclusion and perspectives

A 2D granular fault gouge model has been implemented in the framework of DEM in order to establish a link between gouge properties and rheological behaviour. The combination of cohesion and initial porosity plays a role in the internal structure and geometry of the gouge with pore spaces reduction (from mid-dense to dense sample) and change in particle size repartition (agglomerates formed by the increase of cohesion). A wide range of mechanical behaviours have been observed and compared to current fault gouge rupture theory. In the range of numerical experiment tested

(normal stress 40 MPa, slip rate 1m/s), the increase of cohesion within the gouge leads to an increase of friction peak. The peak strength is sharp, short, and intense for dense and highly cohesive cases and smooth, delayed and of moderate amplitude for mid-dense and moderately cohesive cases. Increasing cohesion also reduces the slip distance at which friction peak is observed and the peak duration (between 25% and 100% of cohesion).

The study of macroscopic friction and gouge kinematics drove us to the identification of main energy sinks in fracture mechanisms. Gouge rupture is led by friction at the interface, by sample dilation and by rupture of cohesive links between particles. In order to take into account these three mechanisms and to see the influence of each contribution seperately, a new model of macroscopic friction has been proposed. It is observed that dilation contribution remains very important in fault gouge fracture and it is a key parameter to identify zones of high-energy release.

The mildly cohesive regime (cohesion lower than 25%) presents a limited influence of cohesion in the rupture mechanisms. The pre-peak phase is very important and is mainly driven by dilatancy. The consequences of this early dilation is that grains reorganization begins in the pre-peak phase allowing an inclination of force chains at 45° at friction peak. This regime is compared to Couette shearing with a ductile behaviour. The ultra-cohesive regime (cohesion larger than 75%) is similar to brittle behaviour, in which Riedel bands are formed and pre-peak phase is negligible. These Riedel bands appear with the beginning of dilatancy and shear localization comes at dilatancy friction peak. We also notice for these highly dense and cohesive samples, the separation of the gouge into two layers: a granular-fluid top layer (shear localization with wear material) and a solid-like bottom layer (cohesive band almost not evolves with slip distance). In between, the cohesive regime (cohesion between 25 and 75%) is a transitory regime between the mildly and the ultra-cohesive regimes, a granular flow with a semi brittle behaviour. A denser rock presents a more localized and brittle mechanical behaviour than a loose sample. Indeed, Riedel shear bands creation are directly linked by the importance of the dilation phase, depending itself on the initial porosity present within the sample.

Mildly cohesive regimes have brought to light the importance or a pre-peak breakdown energy, poorly studied in literature. This pre-peak energy can be neglected, in contrast, for ultra-cohesive regimes. Local Breakdown energy can vary by a factor four along a fault, as this energy depends on the specific history of motion and dynamic stress changes (Lambert & Lapusta, 2020).

The derived slip-weakening law could be implemented in dynamic rupture modelling at higher scale for a dialog with seismological data. In future studies, it could be interesting to update the model to include an explicit dependency to normal stress and slip rates. Depending on the model, contact laws and phenomena studied, other contributions could be added to the friction decomposition proposed.

## Acknowledgements and Data Availability Statement

We thank Arnold Blaisonneau and Julie Maury from BRGM (France) for fruitfull discussions. This study was funded by INSA de Lyon, ministerial grant led by A. Daouadji. The authors declare that they have no competing financial interests. Numerical data and software used for this research are available in these in-text data citation references: Casas et al. (2020), "Cohesion and Initial Porosity of Granular Fault Gouges", Mendeley Data, V1, doi: 10.17632/7c3dcj7spw.1. Other explanations are included in this paper and its supporting information file or available by contacting the corresponding author at nathalie.casas@insa-lyon.fr (Nathalie Casas).

Temporary link to access to the repository:

https://data.mendeley.com/datasets/7c3dcj7spw/draft?a=6df90d11-ba3e-4a65-9521-180304e1dade

## References

Abercrombie, R. E., & Rice, J. R. (2005). Can observations of earthquake scaling constrain slip weakening ? *Geophysical Journal International*, *162*(2), 406–424. https://doi.org/10.1111/j.1365-246X.2005.02579.x

An, L.-J., & Sammis, C. (1994). Particle Size Distribution of Cataclastic Fault Materials from Southern California : a 3D study. *Pure and Applied Geophysics*, *143*(1), 203–227.

Anthony, J. L., & Marone, C. (2005). Influence of particle characteristics on granular friction. *Journal of Geophysical Research: Solid Earth*, *110*(8), 1–14. https://doi.org/10.1029/2004JB003399

Biegel, R. L., Sammis, C. G., & Dieterich, J. H. (1989). The frictional properties of a simulated gouge having a fractal particle distribution. *Journal of Structural Geology*, *11*(7), 827–846.

https://doi.org/10.1016/0191-8141(89)90101-6

Billi, A. (2005). Grain size distribution and thickness of breccia and gouge zones from thin (<1 m) strike-slip fault cores in limestone. *Journal of Structural Geology*, *27*(10), 1823–1837. https://doi.org/10.1016/j.jsg.2005.05.013

Billi, A., & Storti, F. (2004). Fractal distribution of particle size in carbonate cataclastic rocks from the core of a regional strike-slip fault zone. *Tectonophysics*, *384*(1–4), 115–128. https://doi.org/10.1016/j.tecto.2004.03.015

Blenkinsop, T. G. (1991). Cataclasis and Processes of Particle Size Reduction. *Pure and Applied Geophysics*, *136*(1), 59–86.

Byerlee, J. D., & Brace, W. F. (1968). Stick slip, stable sliding, and earthquakes-Effect of rock type, pressure, strain rate, and stiffness. *Journal of Geophysical Research*, *73*(18), 6031–6037. https://doi.org/10.1029/JB073i018p06031

Chester, J. S., Chester, F. M., & Kronenberg, A. K. (2005). Fracture surface energy of the Punchbowl fault, San Andreas system. *Nature*, *437*(7055), 133–136. https://doi.org/10.1038/nature03942

Cho, N., Martin, C. D., & Sego, D. C. (2007). A clumped particle model for rock. *International Journal of Rock Mechanics and Mining Sciences*, *44*(7), 997–1010. https://doi.org/10.1016/j.ijrmms.2007.02.002

Cho, N., Martin, C. D., & Sego, D. C. (2008). Development of a shear zone in brittle rock subjected to direct shear. *International Journal of Rock Mechanics and Mining Sciences*, *45*(8), 1335–1346. https://doi.org/10.1016/j.ijrmms.2008.01.019

Cundall, P. A. ., & Strack, O. D. L. (1979). A discrete numerical model for granular assemblies. *Géotechnique*, *29*(1), 47–65. https://doi.org/10.1680/geot.1979.29.1.47

Da Cruz, F., Emam, S., Prochnow, M., Roux, J. N., & Chevoir, F. (2005). Rheophysics of dense granular materials: Discrete simulation of plane shear flows. *Physical Review E*, *72*(2), 1–17. https://doi.org/10.1103/PhysRevE.72.021309

Daouadji, A., & Hicher, P. (2010). An enhanced constitutive model for crushable granular materials. *International Journal for Numerical and Analytical Methods in Geomechanics*,

*34*, 555–580. https://doi.org/10.1002/nag

Daouadji, A., Hicher, P., Rahma, A., Daouadji, A., Hicher, P., & Rahma, A. (2001). An elastoplastic model for granular materials taking into account grain breakage. *European Journal of Mechanics - A/Solids*, *20*(1), 113–137. https://doi.org/10.1016/S0997-7538(00)01130-X

Di Toro, Giulio, Hirose, T., Nielsen, S., Pennacchioni, G., & Shimamoto, T. (2006). Natural and Experimental Evidence of Melt Lubrication of Faults During Earthquakes. *SCIENCE*, *311*(5761), 647–649. https://doi.org/10.1126/science.1121012

Dorostkar, O., Guyer, R. A., Johnson, P. A., Marone, C., & Carmeliet, J. (2017a). On the micromechanics of slip events in sheared, fluid-saturated fault gouge. *Geophysical Research Letters*, *44*(12), 6101–6108. https://doi.org/10.1002/2017GL073768

Dorostkar, O., Guyer, R. A., Johnson, P. A., Marone, C., & Carmeliet, J. (2017b). On the role of fluids in stick-slip dynamics of saturated granular fault gouge using a coupled computational fluid dynamics-discrete element approach. *Journal of Geophysical Research: Solid Earth*, *122*(5), 3689–3700. https://doi.org/10.1002/2017JB014099

Faulkner, D. R., Mitchell, T. M., Rutter, E. H., & Cembrano, J. (2008). On the structure and mechanical properties of large strike-slip faults. *Geological Society, London, Special Publications*, *299*, 139–150. https://doi.org/10.1144/SP299.9

Ferdowsi, B. (2014). *Discrete element modeling of triggered slip in faults with granular gouge Application to dynamic earthquake triggering* [ETH Zurich]. https://doi.org/10.3929/ethz-a-010232908

Ferdowsi, B., Griffa, M., Guyer, R. A., Johnson, P. A., Marone, C., & Carmeliet, J. (2014). Three-dimensional discrete element modeling of triggered slip in sheared granular media. *Physical Review E*, *89*(4), 1–12. https://doi.org/10.1103/PhysRevE.89.042204

Friedman, M., Handin, J., & Alani, G. (1972). Fracure-surface energy of rocks. *International Journal of Rock Mechanics and Mining Sciences & Geomechanics*, *9*(6), 757–764. https://doi.org/10.1016/0148-9062(72)90034-4

Frye, K. M., & Marone, C. (2003). The effect of particle dimensionality on Granular friction in laboratory shear zones. *Geophysical Research Letters*, *29*(19), 22-1-22–24.

https://doi.org/10.1029/2002gl015709

Gao, K., Euser, B. J., Rougier, E., Guyer, R. A., Lei, Z., Knight, E. E., Carmeliet, J., & Johnson, P. A. (2018). Modeling of Stick-Slip Behavior in Sheared Granular Fault Gouge Using the Combined Finite-Discrete Element Method. *Journal of Geophysical Research: Solid Earth*, *123*(7), 5774–5792. https://doi.org/10.1029/2018JB015668

GRD Midi. (2004). On dense granular flows. *European Physical Journal E*, *14*(4), 341–365. https://doi.org/10.1140/epje/i2003-10153-0

Guo, Y., & Morgan, J. K. (2004). Influence of normal stress and grain shape on granular friction: Results of discrete element simulations. *Journal of Geophysical Research: Solid Earth*, *109*(B12). https://doi.org/10.1029/2004JB003044

Iordanoff, I., Fillot, N., & Berthier, Y. (2005). Numerical study of a thin layer of cohesive particles under plane shearing. *Powder Technology*, *159*(1), 46–54. https://doi.org/10.1016/j.powtec.2005.05.053

Kanamori, H., & Heaton, T. H. (2000). Microscopic and Macroscopic Physics of Earthquakes. In J. B. Rundle, D. L. Turcotte, & W. Klein (Eds.), *Geocomplexity and the Physics of Earthquakes* (pp. 147–163). https://doi.org/10.1029/GM120p0147

Kanamori, H., & Rivera, L. (2006). Energy partitioning during an earthquake. In *Earthquakes: Radiated Energy and the Physics of faulting* (Vol. 170, pp. 3–13). https://doi.org/10.1029/170GM03

Katz, Y., Weinberger, R., & Aydin, A. (2004). Geometry and kinematic evolution of Riedel shear structures, Capitol Reef National Park, Utah. *Journal of Structural Geology*, *26*(3), 491–501. https://doi.org/10.1016/j.jsg.2003.08.003

Lade, P. V, & Overton, D. D. (1989). Cementation Effects in Frictional Materials. *Journal of Geotechnic Engineering*, *115*(10), 1373–1387. https://doi.org/10.1061/(ASCE)0733-9410(1989)115:10(1373)

Lambert, V., & Lapusta, N. (2020). Rupture-dependent breakdown energy in fault models with thermo-hydro-mechanical processes. *Solid Earth Discuss*, *in review*. https://doi.org/10.5194/se-2020-115

Lin, A. (1999). S-C cataclasite in granitic rock. *Tectonophysics*, *304*(3), 257–273. https://doi.org/10.1016/S0040-1951(99)00026-8

Mair, K., Frye, K. M., & Marone, C. (2002). Influence of grain characteristics on the friction of granular shear zones. *Journal of Geophysical Research: Solid Earth*, *107*(B10), ECV 4-1-ECV 4-9. https://doi.org/10.1029/2001JB000516

Mair, K., & Marone, C. (1999). Friction of simulated fault gouge for a wide range of velocities and normal stresses. *Journal of Geophysical Research: Solid Earth*, *104*(B12), 28899–28914. https://doi.org/10.1029/1999JB900279

Marone, C., & Scholz, C. H. (1989). Particle-size distribution and microstructures within simulated fault gouge. *Journal of Structural Geology*, *11*(7), 799–814. https://doi.org/10.1016/0191-8141(89)90099-0

Mollon, G. (2016). A multibody meshfree strategy for the simulation of highly deformable granular materials. *International Journal for Numerical Methods in Engineering*, *108*(12), 1477–1497. https://doi.org/10.1002/nme.5258

Mollon, G. (2018a). A unified numerical framework for rigid and compliant granular materials. *Computational Particle Mechanics*, *5*, 517–527. https://doi.org/10.1007/s40571-018-0187-6

Mollon, G. (2018b). Mixtures of hard and soft grains: micromechanical behavior at large strains. *Granular Matter*, *20*(39). https://doi.org/10.1007/s10035-018-0812-3

Mollon, G. (2019). Solid Flow Regimes Within Dry Sliding Contacts. *Tribology Letters*, *67*(120). https://doi.org/10.1007/s11249-019-1233-0

Mollon, G., Quacquarelli, A., Andò, E., & Viggiani, G. (2020). Can friction replace roughness in the numerical simulation of granular materials? *Granular Matter*, *22*(42). https://doi.org/10.1007/s10035-020-1004-5

Mollon, G., & Zhao, J. (2012). Fourier-Voronoi-based generation of realistic samples for discrete modelling of granular materials. *Granular Matter*, *5*, 621–638. https://doi.org/10.1007/s10035-012-0356-x

Morgan, J. K. (1999). Numerical simulations of granular shear zones using the distinct element method: 2. Effects of particle size distribution and interparticle friction on mechanical

behavior. *Journal of Geophysical Research: Solid Earth*, *104*(B2), 2721–2732. https://doi.org/10.1029/1998jb900055

Morgan, J. K., & Boettcher, M. S. (1999). Numerical simulations of granular shear zones using the distinct element method: 1. Shear zone kinematics and the micromechanics of localization. *Journal of Geophysical Research: Solid Earth*, *104*(B2), 2703–2719. https://doi.org/10.1029/1998jb900056

Muto, J., Nakatani, T., Nishikawa, O., & Nagahama, H. (2015). Fractal particle size distribution of pulverized fault rocks as a function of distance from the fault core. *Geophysical Research Letters*, *42*(10), 3811–3819. https://doi.org/10.1002/2015GL064026

Niemeijer, A., Toro, G. Di, Nielsen, S., & Felice, F. Di. (2011). Frictional melting of gabbro under extreme experimental conditions of normal stress , acceleration , and sliding velocity. *Journal of Geophysical Research*, *116*(B07404). https://doi.org/10.1029/2010JB008181

Nouguier-lehon, C., Cambou, B., & Vincens, E. (2003). Influence of particle shape and angularity on the behaviour of granular materials : a numerical analysis. *International Journal for Numerical and Analytical Methods in Geomechanics*, *27*(14), 1207–1226. https://doi.org/10.1002/nag.314

Ohnaka, M. (2003). *A constitutive scaling law and a unified comprehension for frictional slip failure , shear fracture of intact rock , and earthquake rupture*. *108*, 1–21. https://doi.org/10.1029/2000JB000123

Olgaard, D. L., & Brace, W. F. (1983). The microstructure of gouge from a mining-induced seismic shear zone. *International Journal of Rock Mechanics and Mining Sciences & Geomechanics*, *20*(1), 11–19. https://doi.org/10.1016/0148-9062(83)91610-8

Philit, S., Soliva, R., Castilla, R., Ballas, G., & Taillefer, A. (2018). Clusters of cataclastic deformation bands in porous sandstones. *Journal of Structural Geology*, *114*, 235–250. https://doi.org/10.1016/j.jsg.2018.04.013

Potyondy, D. O., & Cundall, P. A. (2004). A bonded-particle model for rock. *International Journal of Rock Mechanics and Mining Sciences*, *41*(8), 1329–1364. https://doi.org/10.1016/j.ijrmms.2004.09.011

Pouliquen, O. (2011). Granular Flow. In B. Duplantier, T. Halsey, & V. Rivasseau (Eds.),

*Glassses and Grains. Progress in Mathematical Physics, vol 61* (pp. 77–109). Springer. https://doi.org/10.1007/978-3-0348-0084-6_4

Rathbun, A. P., Renard, F., & Abe, S. (2013). Numerical investigation of the interplay between wall geometry and friction in granular fault gouge. *Journal of Geophysical Research: Solid Earth*, *118*(3), 878–896. https://doi.org/10.1002/jgrb.50106

Rice, J., & Cocco, M. (2005). Seismic Fault Rheology and Earthquake Dynamics. In M. R. Handy, G. Hirth, & N. Hovius (Eds.), *The Dynamics of Fault Zones* (Dahlem Wor, pp. 99–137). MIT Press.

Rice, J. R. (2006). Heating and weakening of faults during earthquake slip. *Journal of Geophysical Research: Solid Earth*, *111*(5), 1–29. https://doi.org/10.1029/2005JB004006

Rognon, P. G., Roux, J. N., Naaïm, M., & Chevoir, F. (2008). Dense flows of cohesive granular materials. *Journal of Fluid Mechanics*, *596*, 21–47. https://doi.org/10.1017/S0022112007009329

Rowe, P. W. (1962). The stress-dilatancy relation for static equilibrium of an assembly of particles in contact. *F.R.S*, *269*(1339). https://doi.org/https://doi.org/10.1098/rspa.1962.0193

Sammis, C. G., & Biegel, R. L. (1989). Fractals, Fault-Gouge, and Friction. *Pure and Applied Geophysics*, *131*, 255–271. https://doi.org/10.1007/BF00874490

Sammis, C., King, G., & Biegel, R. (1987). The kinematics of gouge deformation. *Pure and Applied Geophysics*, *125*, 777–812. https://doi.org/10.1007/BF00878033

Schellart, W. P. (2000). Shear test results for cohesion and friction coe ffi cients for di ff erent granular materials : scaling implications for their usage in analogue modelling. *Tectonophysics*, *324*(l–2), 1–16. https://doi.org/10.1016/S0040-1951(00)00111-6

Scholz, C. H. (2002). *The Mechanics of Earthquakes and Faulting, second edition* (Cambridge). https://doi.org/10.2113/gseegeosci.13.1.81

Sone, H., & Shimamoto, T. (2009). Frictional resistance of faults during accelerating and decelerating earthquake slip. *Nature Geoscience*, *2*(10), 705–708. https://doi.org/10.1038/ngeo637

Tchalenko, J. S. (1970). Similarities between shear zones of different magnitudes. *Geological*

*Society Of America Bulletin*, *81*(6), 1625–1640. https://doi.org/10.1130/0016-7606(1970)81[1625:SBSZOD]2.0.CO;2

Toro, G Di, Han, R., Hirose, T., Paola, N. De, Nielsen, S., Mizoguchi, K., Ferri, F., Cocco, M., & Shimamoto, T. (2011). Fault lubrication during earthquakes. *Nature*, *471*, 494–498. https://doi.org/10.1038/nature09838

Zhao, Z., Jing, L., & Neretnieks, I. (2012). Particle mechanics model for the effects of shear on solute retardation coefficient in rock fractures. *International Journal of Rock Mechanics and Mining Sciences*, *52*, 92–102. https://doi.org/10.1016/j.ijrmms.2012.03.001

*Submitted for publication in Journal of Geophysical Research : Solid Earth*

Supporting Information for

# Cohesion and Initial Porosity of Granular Fault Gouges control the Breakdown Energy and the Friction Law at the Onset of Sliding

N. Casas [1,2*], G. Mollon[1], and A. Daouadji[2]

1 Univ. Lyon, INSA-Lyon, CNRS UMR5259, LaMCoS, F-69621, France.
2 Univ. Lyon, INSA-Lyon, GEOMAS, F-69621, France.]

Corresponding author: Nathalie Casas (nathalie.casas@insa-lyon.fr)

## Contents of this file



## Additional Supporting Information (Files uploaded separately)



## Introduction

The following paragraphs present: (S1) the numerical setup and parameters used in the study for direct shear experiment, (S2) the methodology and results allowing to determine the Representative Surface Element (RSE), (S3) the method used to compute the initial porosity selected for numerical modelling (i.e. dense and mid-dense sample), (S4) how to pass from a numerical cohesion to a percentage of cohesion within the gouge, (S5) tables of main results of DEM modelling and gouge kinematics, (S6) the formula used to calculate the energy consumption during numerical experiments, (S7) detailed and validation for the proposed simplified model.

## S1. Numerical setup and parameters for direct shear experiment

S1.1: 2D Numerical granular sample

Paking2D downloadable here.

**Table S1**. Parameters used for grain generation.

| Property | Value |
|---|---|
| Distribution type | fractal |
| Parameter of distribution | D=2.6 |
| Sample size | 2 x 20 mm |

S1.2: 2D Direct shear experiment with DEM

MELODY 2D downloadable here.

**Table S2**. Numerical properties for direct shear experiment.

| Property | Value |
|---|---|
| Normal stress | 40 MPa |
| Shear velocity | 1 m/s |
| Volumetric mass | 2600 Kg/m3 (grains)<br>26 Kg/m3 (rock walls) |
| Numerical stiffness | 1E+15 $N/m^3$ |
| Inter-particular friction | 0.5 |
| Sample size | 2 x 20 mm |
| Number of particles | 4960 |

**Table S3**. Numerical setup and solver

| Property | Value |
|---|---|
| Constant time step (Euler scheme) | 1e-9 s |
| Contact updating period | 1e-7 s |

## S2. Representative Surface Element (RSE)

In order to justify a RSE, three different sizes of model have been studied with identical numerical parameters. The differences sizes of models (6x2mm², 10x2mm² and 20x2 mm²) induce a change in the total number of particles in order to keep the same equivalent diameter for grains (respectively 1500, 2500 and 5000 grains). By increasing the number of grains in the model as well as the length of the gouge, we observe similar behaviours of the sheared gouge layers. Friction coefficient follows the same trend for the three size of model. The friction peak $\mu_p$ is of the same order of magnitude (0.73-0.78). A small difference is observed for the case with 2500 grains, where the friction peak is more important, probably due to a slightly different stacking of the particles during the compaction of the sample (Figure S1). As the number of grains increases, there is therefore an increase in normal and tangential forces applied to the upper rock wall. The number of grains is higher, but the gouge size also increases, making possible to maintain a similar coefficient of friction in the three models. The friction curve obtained with the 1500-grains sample are noisier, because the dynamic effects are more noticeable with fewer grains. However, by comparing force chains in the gouge for the three models, we do not see significant changes (Figure S2 – a). They are oriented at 30-45 ° relatively to the upper rock wall and normal forces seem oriented in this same direction (Figure S2 –b). Using 5000 grains seems to give a sufficiently representative behaviour to observe local mechanisms. It is therefore not necessary to represent a larger model for this type of micromechanical study.

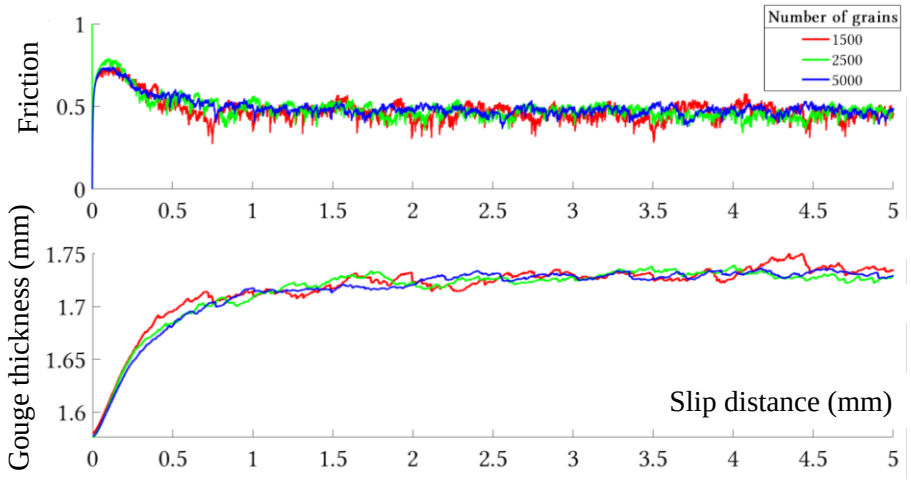


**Figure S1.** Friction coefficient and gouge thickness (mm) as functions of the slip distance (mm), small sample with 1500 particles in red, middle-size sample with 2500 particles in green and large sample used in the paper with 5000 grains in blue.

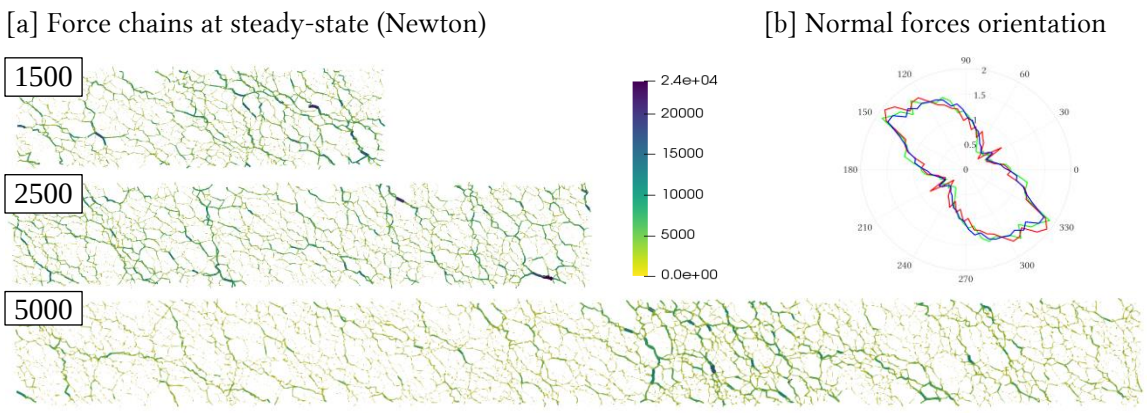


**Figure S2**. [a] Force chains magnitude in Newton for 1500 grains, 2500 grains and 5000 grains – [b] Number of contacts with a normal vector oriented in a given direction (using polar diagrams where the Theta-axis is the orientation and the R-axis is the number of contacts), Normal forces orientation as a function of the model, at steady state. Small sample with 1500 particles in red, the middle sample with 2500 particles in green and the sample used in the paper with 5000 grains in blue.

## S3. Initial porosity and intergranular friction

To have an evolution of the initial porosity inside gouge samples, we compacted eleven samples with inter-particle friction coefficients between 0 and 1, allowing to obtain more or less dense grain stacks. With a zero inter-particle friction coefficient, the only contact parameter between grains is the numerical stiffness. The packing obtained is in a very dense state, with a solid fraction close to 0.89 (i.e. porosity of 0.11). In the opposite, adding a friction coefficient of 1 between each contact hinders movements and contacts and results in a much less dense sample (0.83). The idea is, therefore, to see the influence of this initial state on gouge shearing. The compaction of samples was carried out on a sample of 4960 grains generated according to a fractal distribution law (dimension factor D = 2.6), i.e. with the same initial sample before compaction step. Parameters used for samples compaction are written in Table S2.

Eleven samples were created and solid fraction was measured at the end of the compaction step. The solid fraction ($F_S$) is the ratio of the surface occupied by the grains to the apparent surface of the sample. Since we are here in 2D, we will take an area rather than a volume considering that the 3$^{rd}$ dimension is the same in the numerator and denominator. In the associated paper, we talk about the percentage of porosity (i.e. the ratio of the surface

occupied by voids to the apparent surface of the sample) rather than solid fraction. The solid fraction and porosity in a sample can therefore be calculated as follows, with S an area:

$$F_S = \frac{S_{grains}}{S_{gouge}} \quad (1)$$

$$S_{gouge} = S_{grains} + S_{void} \quad (2)$$

$$P_S = \frac{S_{voids}}{S_{gouge}} \quad (3)$$

Figure S3 displays the solid fraction and gouge thickness (mm) for each sample generated with a different inter-particle friction coefficient. We observe that gouge thickness decreases with the increase of solid fraction. The highest solid faction (0.89) corresponds to a very dense sample in which there is very few porosity between grains. In contrast, the lowest solid fraction (0.83) corresponds to a slightly less dense sample, with a gouge thickness of 0.12 mm greater, (5% of the total thickness). We can see the representation of this solid fraction in Figure S4. Samples used in the associated paper are sample 10 ($F_S$=0.89 or Ps=11%) and 15 ($F_S$=0.84 or Ps=16%).

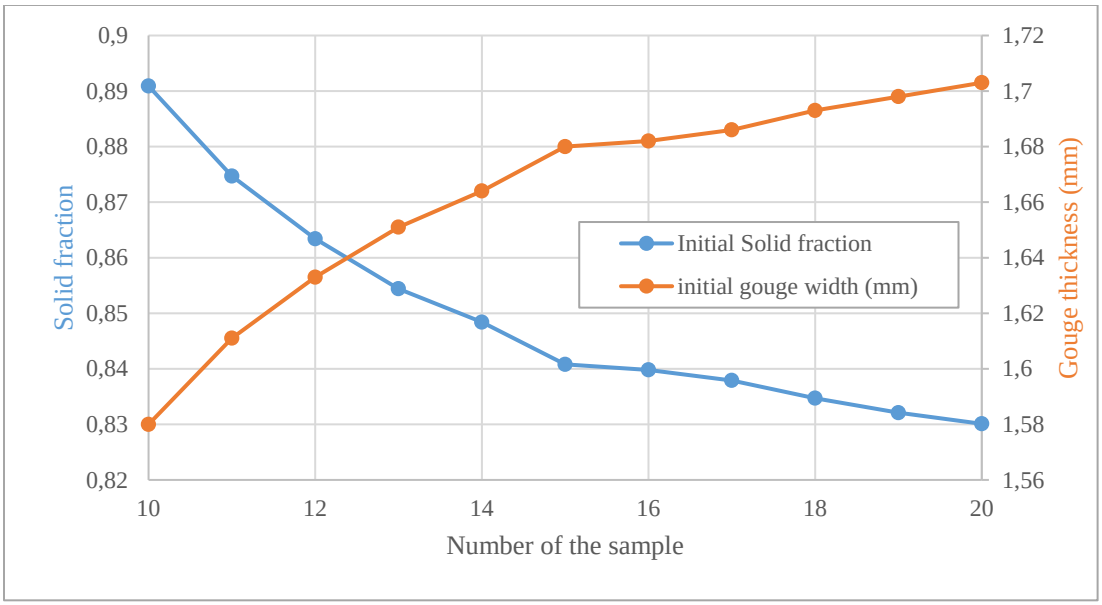


**Figure S3**. Evolution of solid fraction (in blue) and gouge thickness (in orange) as a function of the inter-particle friction used to compact samples (replaced by a sample number). The sample 10 corresponds to a zero friction and the 20 to a friction equal to one.

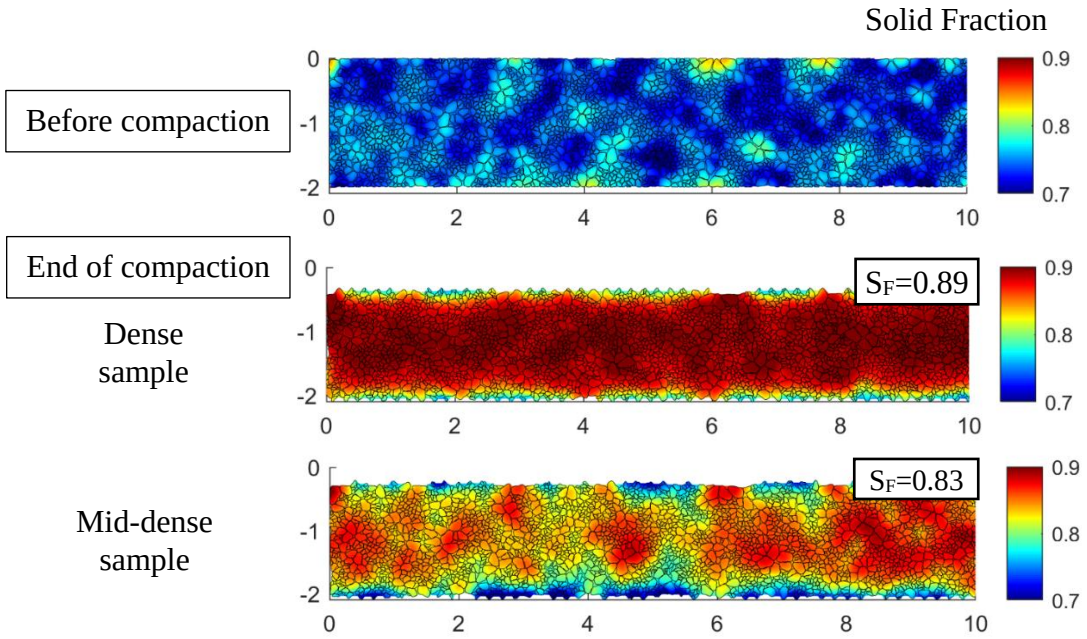


**Figure S4.** Solid fraction at different step of the simulation – half of a fault segment (0 -10mm). The first line displays the initial solid fraction before compaction (solid fraction between 0.7 and 0.8). At the end of compaction, we can clearly distinguish the difference between a very dense sample, with a homogeneous and high solid fraction over the entire gouge (i.e. lower porosity of 11%) and a mid-dense sample with an less homogeneous solid fraction (i.e. higher porosity of 17%), which depends on the stacks of grains created during the compaction.

## S4. Percentage of cohesion within the gouge

To quantify the total amount of cohesion energy in the initial state of the fault (i.e. the energy that would be needed in order to break all the initial bonds), we normalize it with respect to a representative energy. This quantity corresponds to a surface energy of 62J/m² (reported for the Chilhowee quartzite and considered as an upper limit for rock surface energy in (Friedman et al., 1972)) applied on the whole external surface of all the grains present in the simulation (a unit length is considered in the third dimension for any necessary purpose). This would correspond to 100% of cohesion, and we explore the influence of this percentage in the paper (Figure 3 – c). Detailed calculi are explained in this Section.

The maximal energy for a fault patch of 1m² and for cemented bonds covering the total external surface of all particles in the gouge can be written as:

$$E_{max} = 2U\frac{P_{tot}}{L_{gouge}} \tag{4}$$

With U = 62J/m², $P_{tot}$ the sum of the perimeter of all grains in [m] and $L_{gouge}$ the length of the fault model in [m]. In our model, the energy to break all cohesive bonds on a 1m² fault patch can be defined as $E_C\ (J/m^2)$, the energy of de-cohesion, representing the energy needed by the system to break all cohesive bonds initially present in the gouge. It can be described by a relation between properties of the initial contact network (cumulated length of all the contacts $L_{intact-tot}$ and number $n$ of contacts, stiffness $k$), and the initial numerical cohesion $C_{num}$ for each contact and the length $L_{gouge}$ of the model:

$$E_C = L_{intact-tot}\left(\frac{C_{num}}{2}\right)^2\frac{1}{2\,k\,L_{gouge}} \tag{5}$$

Supposing that the maximum apparent surface energy needed by the gouge to break a bond is $E_{max}$, for a fully cemented material. We determine the value $C_{num-100\%}$ of numerical cohesion, which corresponds to a cohesion of 100% based on the definition given above. We can thus express the cohesive energy in our initial sample as a percentage of cohesion $X\%$ in comparison to the 100% cohesion.

$$E_C = E_{max} \tag{6}$$

$$C_{num-100\%} = \sqrt{\frac{16\, E_{max}\, P_{tot}\, k}{L_{intact-tot}}} \tag{7}$$

$$X\% = \left(\frac{C_{num}}{C_{num-100\%}}\right).100 \tag{8}$$

## S5. Results and Gouge kinematics

Results obtained with numerical setup and properties displayed in Table S2:

**Table S4**. Results for dense samples (initial porosity of 11% or solid fraction SF=0.89). With Δτ (Pa) the stress drop from the friction peak to the plateau, $\mu_{SS}$ the steady-state friction, $\mu_p$ the friction peak, $SF_{SS}$ the steady state solid fraction, $P_{SS}$ the steady-state porosity, $Ep_{SS}$ the steady-state gouge thickness.

| $C_{num}$ | 100 | 200 | 500 | 800 | 1000 | 1200 | 1500 | 2000 | 2500 |
|---|---|---|---|---|---|---|---|---|---|
| % cohesion | 4 | 8 | 19 | 30 | 38 | 46 | 57 | 76 | 95 |
| Δτ (Pa) | 1.08+07 | 1.11E+07 | 1.82E+07 | 3.01E+07 | 3.66E+07 | 4.20E+07 | 5.27E+07 | 6.84E+07 | 8.75E+07 |
| $\mu_{SS}$ | 0.481 | 0.482 | 0.490 | 0.477 | 0.496 | 0.484 | 0.475 | 0.473 | 0.431 |
| $\mu_p$ | 0.771 | 0.786 | 0.994 | 1.406 | 1.695 | 1.938 | 2.376 | 3.094 | 3.838 |
| $SF_{SS}$ | 0.869 | 0.867 | 0.876 | 0.877 | 0.869 | 0.87 | 0.884 | 0.895 | 0.889 |
| $P_{SS}$ | 0.131 | 0.133 | 0.124 | 0.123 | 0.131 | 0.13 | 0.116 | 0.105 | 0.111 |
| $Ep_{SS}$ (mm) | 1.72 | 1.726 | 1.707 | 1.705 | 1.72 | 1.719 | 1.691 | 1.671 | 1.681 |

The representation of the relative damage gives a picture of the state of decohesion between grains and its location within the gouge. This damage is set to 0 when cohesive bonds are first established (all the bonds are intact) and may evolve until 1 if all these bonds reach the "broken" status (cf. Section 2.3 in the associated paper). It is thus a relative damage with respect to an initial state. The following movies illustrate the evolution of the gouge state as a function of the slip distance:

**Movie S1.** Comparison of the evolution of relative damage with slip distance for dense samples (entire granular gouge), between 8% cohesion (mildly cohesive regime) and 38% cohesion (cohesive regime). From zero imposed slip [A] to the beginning of steady state [G].

**Movie S2.** Comparison of the evolution of relative damage with slip distance for dense samples (entire granular gouge), between 38% cohesion (cohesive regime) and 95% cohesion (ultra-cohesive regime). From zero imposed slip [A] to the beginning of steady state [G].

The following movies present the evolution of solid fraction as a function of the slip distance for the three regimes highlighted in the paper. Another way to observe Riedel bands and cracks within the gouge.

**Movie S3.** Solid fraction in dense sample (entire granular gouge) as a function of the slip distance for 8% cohesion (mildly cohesive regime). From zero imposed slip [A] to the beginning of steady state [G].

**Movie S4.** Solid fraction in dense sample (entire granular gouge) as a function of the slip distance for 38% cohesion (cohesive regime). From zero imposed slip [A] to the beginning of steady state [G].

**Movie S5.** Solid fraction in dense sample (entire granular gouge) as a function of the slip distance for 95% cohesion (ultra-cohesive regime). From zero imposed slip [A] to the beginning of steady state [G].

**Table S5**. Results for mid-dense samples (initial porosity of 16% initial solid fraction SF=0.84) With $\Delta\tau$ (Pa) the stress drop from the friction peak to the plateau, $\mu_{SS}$ the steady-state friction, $\mu_p$ the friction peak, $SF_{SS}$ the steady state solid fraction, $P_{SS}$ the steady-state porosity, $Ep_{SS}$ the steady-state gouge thickness.

| $C_{num}$ | *100* | *200* | *500* | *800* | *1000* | *1200* | *1500* | *2000* |
|---|---|---|---|---|---|---|---|---|
| % $cohesion$ | 3 | 6 | 18 | 31 | 40 | 50 | 66 | 95 |
| $\Delta\tau$ *(Pa)* | 3.02E+06 | 2.60E+06 | 3.69E+06 | 9.06E+06 | 1.39E+07 | 1.92E+07 | 2.61E+07 | 3.57E+07 |
| $\mu_{SS}$ | 0.461 | 0.466 | 0.460 | 0.458 | 0.469 | 0.479 | 0.476 | 0.455 |
| $\mu_p$ | 0.536 | 0.531 | 0.552 | 0.684 | 0.815 | 0.959 | 1.130 | 1.346 |
| $SF_{SS}$ | 0.855 | 0.854 | 0.852 | 0.85 | 0.851 | 0.857 | 0.864 | 0.858 |
| $P_{SS}$ | 0.145 | 0.146 | 0.148 | 0.15 | 0.149 | 0.143 | 0.136 | 0.142 |
| $Ep_{SS}$ *(mm)* | 1.749 | 1.752 | 1.756 | 1.766 | 1.757 | 1.745 | 1.73 | 1.742 |

## S6. Energy Budget

The following section presents the energy budget of the model divided into three contributions theoretically described as dilatancy, friction and decohesion (Section 3.3 and 4.1 in the associated paper). Each formula corresponds to one different mechanism. (Figure S5 – a) displays the evolution of energy consumption as a function of the slip distance for all contributions for a dense case with 57% of cohesion. We can also observe the associated friction (Figure S5 – b) used to create simplified models in Section 3.3. (Figure S5 – c & d) helps analysing the percentage of energy consumed in pre-peak phase and the percentage of cohesion remaining in the sample with the increasing slip distance. The total energy is calculated at every time step with the formula bellow.

$$E_{tot}(t) = E_{tot}(t-1) + \frac{[D_x(t) - D_x(t-1)] * [F_x(t) + F_x(t-1)]}{2 * S_{gouge}} \quad (9)$$

With t the current time step, $D_x$ the horizontal displacement of the upper rock wall, $F_x$ the tangential forces acting on the upper rock wall and $S_{gouge} = L_{gouge} * 1$ (2D).

The Dilatancy energy is, at every time step:

$$E_{dilatancy}(t) = \frac{[D_y(t)] * [F_y(t)]}{S_{gouge}} \quad (10)$$

With $D_y$ the vertical displacement of the upper rock wall, $F_y$ the normal forces acting on the upper rock wall.

It is also possible to calculate an averaged post-peak Dilatancy energy :

$$E_{mid-dil} = \left[D_{y_{ss}} - H_{peak}\right] * \sigma_N \quad (11)$$

With $D_{y_{SS}}$ the gouge thickness at steady-state, $H_{peak}$ the gouge thickness at friction peak and $\sigma_N$ the normal stress.

The Decohesion energy at every time step is: (12)

$$E_{damage}(t) = L_{contact} * \left[\frac{C_{num}}{2}\right]^2 * \frac{1}{2k_n} * \frac{1}{S_{gouge}}$$

With $L_{contact}$ the total length of contacting grains, $C_{num}$ the numerical cohesion described in S4 and $k_n$ the numerical stiffness.

Friction and elastic energies at every time step results in the remaining energy of the model:

$$E_{friction}(t) = E_{tot}(t) - E_{dilatancy}(t) - E_{damage}(t) \quad (13)$$

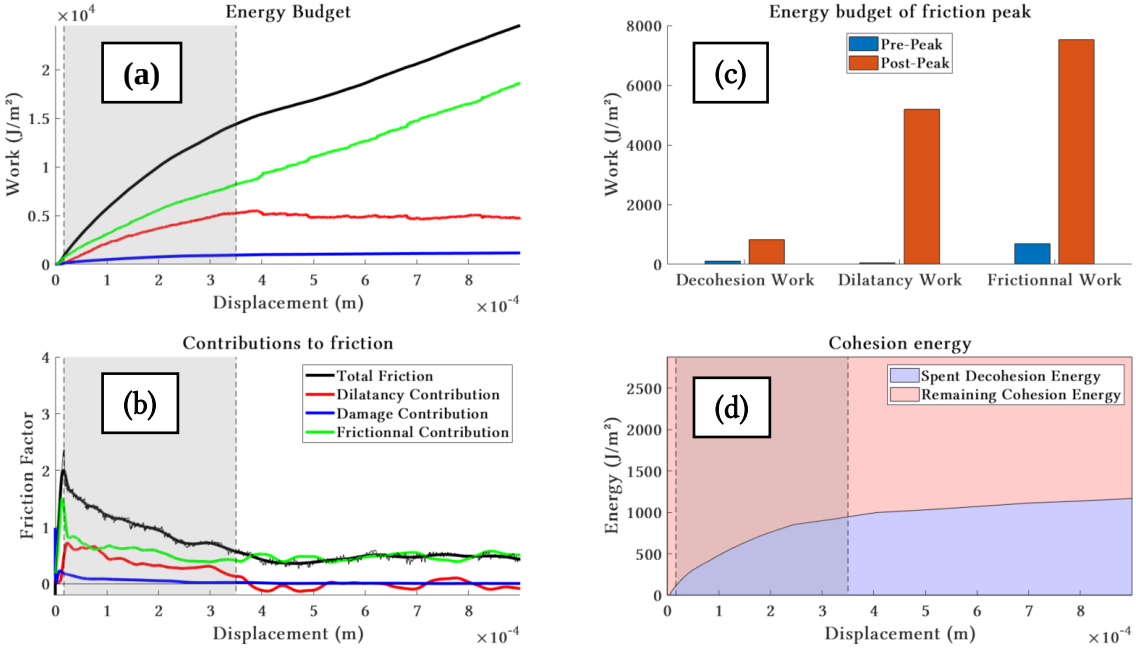


**Figure S5.** Dense sample with 57% of cohesion (a) Energy budget as a function of slip displacement for the different contributions, (b) Friction coefficient extracted from energy consumption, (c) Energy budget in pre-peak or post-peak phase, (d) Cohesion spent and remaining in the sample as a function of the slip distance.

## S7. Simplified model – validation

The Figure S7 (present in the paper) displays the proposed evolution for each parameter used in the simplified models, as a function of the cohesion after fitting on all the simulation data.

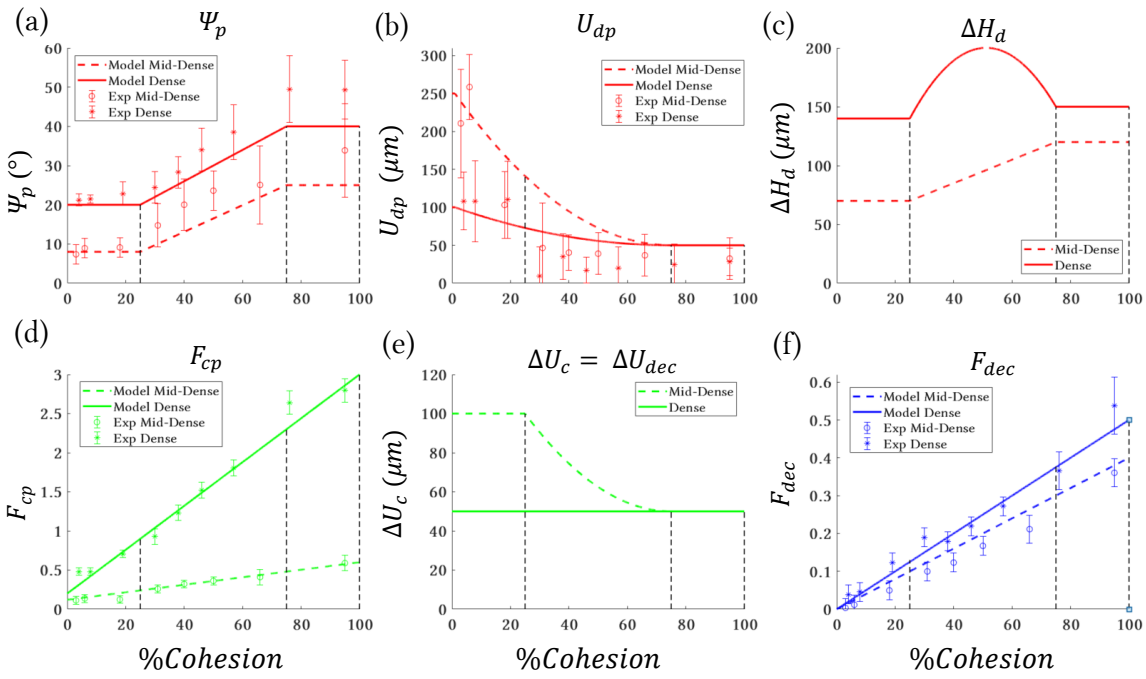


**Figure S6**. Model of friction laws presenting the 7 parameters taken into account in the simplified models. It can be noted that k, $\mu_{SS}$, and $\Delta U_{cpp}$ do not depend on cohesion. (a) Maximum dilatancy angle Ψp. (b) Slip distance corresponding to the maximum dilatancy $U_{dp}$. (c) Gain in gouge thickness at the end of the dilatancy phase $\Delta H_d$. (d) Peak friction at the end of the elastic phase $F_{cp}$ and post peak friction $F_{cpp}$ . (e) Characteristic distance of the exponential decay $\Delta U_c$. (f) Maximum friction induced by decohesion $F_{dec}$. Dots are experimental data derived from DEM modelling. They may be not aligned with numerical modelling as some peak values are difficult to identify on raw data and the error can be important. $\Delta H_d$ and $\Delta U_c$ do not have experimental data, as they are completely created for the model.

Dilatancy parameters are not following linear laws and both mildly and ultra-cohesive regimes present constant values, meaning that the major evolution occurs in the transitional cohesive regime [Figure S6 – a, b, c]. As $\Psi_p$ is increasing with the percentage of cohesion. the slip distance associated to this maximum is reducing. The more cohesion is added, the earlier the maximum dilatancy is observed. These results are consistent with the associated paper related to the main behaviour of the gouge regarding the initiation of sliding. $\Delta H_d$

gives the shape of the Gaussian model. Even though a lognormal law seemed to better fit the dilatancy friction curves than a Gaussian law, it was not satisfactory for global friction models. The objective of this simplified model is not to reproduce the exact location of dilatancy friction peak, but to model a global and consistent shape evolution from one case to another.

Pushing up cohesion increases Coulomb friction peak and post peak friction that follow a linear law (Figure S6 – d). The fact that denser samples have a superior friction peak may be due to the higher number of contacts of each particle that generates more resistance to sliding. The characteristic distance $\Delta U_c$ remains almost constant for dense samples, but decreases for mid-dense samples as a function of the cohesion (Figure S6 – e). This evolution is related to the type of Coulomb model observed: a larger distance of decay for asymptotic models (Figure 13 – d in the paper).

For decohesion contribution, $F_{dec}$ evolves as a rising linear law from 0 to 100% cohesion [Figure S6 – f] in accordance with previous results (Section 3.3 in the paper).

It can be noted that $\Delta U_{cpp}$, $k$ and $\mu_{SS}$ are independent of cohesion and taken as constant. The slip distance $\Delta U_{cpp}$ is equal to 8 µm for dense samples and 40 µm for mid-dense samples. The gouge layer stiffness $k$ is found to be equal to 140 kN/m for dense samples and to 80 kN/m for mid-dense samples.

The Figure S7 below presents the simplified models and the initial curves values. The total friction is the black curve, sum of the contributions of: the dilatancy friction (red), the Coulomb friction (green) and of the decohesion friction (blue). These contributions are calculated thanks to global potential energy recovered at each time step, from the data set presented in previous sections and computations details presented in S1. The detailed model is presented in Section 2 in the paper. Six chosen cases are presented here to validate the experimental friction curves with the friction decomposition proposed: one case for each regime described in Section 3.2 (mildly cohesive, cohesive and ultra-cohesive) and for each type of compacted sample (dense and mid-dense).

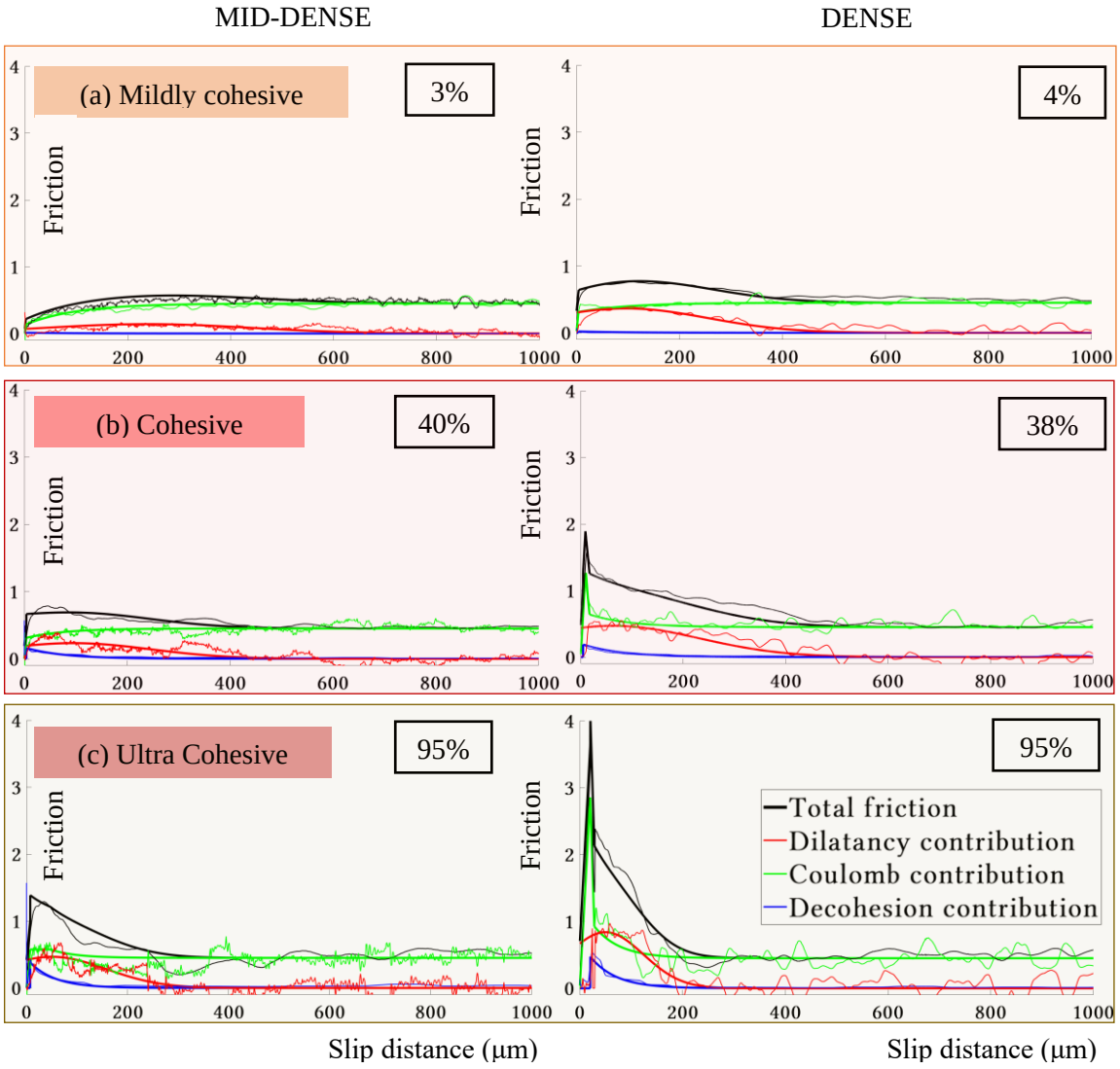


**Figure S7.** Mid-dense and dense models – validation as a function of the percentage of cohesion. Friction-slip curve with different contributions (dilatancy in red, Coulomb in green and decohesion in blue), the black curve is the sum of all contributions. (a) mildly cohesive regimes, where the observed pre-peak phase is important - (b) Cohesive regimes with a diminution of the pre-peak phase with the increase of cohesion - (c) Ultra cohesive regimes with almost no pre-pic phase.